

Identifications of Faint *Chandra* Sources in the Globular Cluster M3

Yue Zhao¹, Craig O. Heinke¹, Haldan N. Cohn², Phyllis M. Lugger², Adrienne M. Cool³

¹Department of Physics, University of Alberta, CCIS 4-183, Edmonton, AB T6G 2E1, Canada

²Department of Astronomy, Indiana University, 727 E. Third St., Bloomington, IN 47405, USA;

³Department of Physics and Astronomy, San Francisco State University, 1600 Holloway Avenue, San Francisco, CA 94132, USA

Accepted XXX. Received YYY; in original form ZZZ

ABSTRACT

We report a 30 ks *Chandra* ACIS-S survey of the globular cluster M3. Sixteen X-ray sources were detected within the half-light radius (2.3') with $L_X \gtrsim 2.3 \times 10^{31}$ erg s⁻¹. We used *Hubble Space Telescope* WFC3/UVIS and ACS/WFC images to find 10 plausible optical/UV counterparts. We fit the spectral energy distribution of the known cataclysmic variable 1E1339.8+2837 with a blue ($T_{\text{eff}} = 2.10_{-0.58}^{+1.96} \times 10^4$ K, 90% conf.) spectral component from an accretion disc, plus a red component ($T_{\text{eff}} = 3.75_{-0.15}^{+1.05} \times 10^3$ K) potentially from a subgiant donor. The second brightest source (CX2) has a soft blackbody-like spectrum suggesting a quiescent low-mass X-ray binary (qLMXB) containing a neutron star. Six new counterparts have obvious UV and/or blue excesses, suggesting a cataclysmic variable (CV) or background active galactic nucleus (AGN) nature. Two (CX6 and CX8) have proper motions indicating cluster membership, suggesting a CV nature. CX6 is blue in UV filters but red in V-I, which is difficult to interpret. Two CV candidates, CX7 and CX13, show blue excesses in B-V colour but were not detected in the UV. The other two CV candidates were only detected in the two UV bands (UV₂₇₅ and NUV₃₃₆), so do not have proper motion measurements, and may well be AGNs. One *Chandra* source can be confidently identified with a red straggler (a star redward of the giant branch). The observed X-ray source population of M3 appears consistent with its predicted stellar interaction rate.

Key words: globular clusters: individual (M3) – X-ray: binaries – novae, cataclysmic variables – stars: neutron

1 INTRODUCTION

Galactic globular clusters (GCs) are gravitationally-bound dense and old stellar populations harbouring $\sim 10^4 - 10^6$ stars. The high stellar density in the core region leads to many stellar encounters, and therefore creates a favourable environment to form a variety of close binary systems through dynamical processes (e.g. Fabian et al. 1975; Hills 1976; Camilo & Rasio 2005; Ivanova et al. 2006). Bright X-ray binaries ($L_X \sim 10^{36-37}$ erg s⁻¹) in globular clusters are transient or persistent low-mass X-ray binaries (LMXBs) typically harbouring accreting neutron stars (NSs) with low-mass optical companions (Lewin & Joss 1983; Grindlay et al. 1984). These LMXBs are clearly produced dynamically, based on their association with the densest globular clusters in our Galaxy (Clark 1975; Verbunt & Hut 1987; Verbunt 2003) and in other galaxies (Jordán et al. 2004;

Sivakoff et al. 2007; Jordán et al. 2007; Peacock et al. 2009). High angular resolution X-ray observations with *Chandra* have revealed large numbers of faint ($L_X \sim 10^{29-34}$ erg s⁻¹) X-ray sources in globular clusters (Verbunt & Lewin 2006; Heinke et al. 2010). The faint X-ray population is composed of multiple source classes, including: quiescent low-mass X-ray binaries (qLMXBs) in which accretion onto the NS is thought to be stopped or at least largely suppressed (Campana et al. 1998; Rutledge et al. 2002; Heinke et al. 2003; Chakrabarty et al. 2014) with luminosities typically $\sim 10^4$ times fainter than during outbursts; cataclysmic variables (CVs) where white dwarfs accrete from low-mass companions (Hertz & Grindlay 1983; Cool et al. 1995; Pooley et al. 2002; Cohn et al. 2010; Rivera Sandoval et al. 2018); millisecond pulsars (MSPs), thought to be radio pulsars that have been spun up by accretion (Bhattacharya & van den Heuvel 1991), which are observed in both X-ray (Saito et al. 1997; Bogdanov et al. 2006) and radio (Ransom et al. 2005; Freire et al. 2017); and chromospherically active binaries

* E-mail: zhao13@ualberta.ca

(ABs) composed of two tidally-locked non-degenerate stars, wherein fast rotation induces active coronal regions that emit (relatively faint, $L_X < 10^{31}$ erg s $^{-1}$) X-rays (Bailyn et al. 1990; Dempsey et al. 1993; Grindlay et al. 2001; Heinke et al. 2005b). The qLMXBs and CVs appear to be correlated with encounter rate (Pooley et al. 2003; Heinke et al. 2003; Pooley & Hut 2006; Bahramian et al. 2013), while the ABs are expected to be primordial in origin (Bassa et al. 2004; Verbunt et al. 2008; Bassa et al. 2008; Lu et al. 2009; Huang et al. 2010).

The globular cluster M3 (or NGC 5272) is a good target to study for several reasons. First, M3 is massive, but has a relatively low core density (central luminosity $\rho_c \approx 3.7 \times 10^3 L_\odot$ pc $^{-3}$ according to Harris 1996, 2010 version), which suggests a relative predominance of primordially, over dynamically, formed X-ray binaries (XRBs). Moreover, a less dense core facilitates the optical identification of counterparts to X-ray sources, which is difficult in denser clusters due to crowding. The X-ray sources in M3 also show a relatively dispersed distribution, which allows easier identifications and also makes them good targets for future X-ray observations with instruments that have larger collecting area but relatively larger PSFs (e.g. XMM-Newton, and the future telescope Athena). Secondly, M3's position far from the Galactic Plane means it suffers relatively little reddening, making photometric studies easier and more precise. This will, in turn, support the identification of possible counterparts.

Previous X-ray studies of M3 have focused on the brightest X-ray source, 1E1339.8+2837 (1E1339 hereafter). 1E1339 was first discovered as a faint X-ray source ($L_X \sim 10^{33}$ erg s $^{-1}$) by the *Einstein Observatory* (Hertz & Grindlay 1983). It underwent a bright outburst observed by ROSAT in 1991–1992, during which it showed a very soft spectrum ($kT \approx 20 - 45$ eV, $L_X \sim 10^{35}$ erg s $^{-1}$, Hertz et al. 1993; Verbunt et al. 1995). The source returned back to quiescence with a much harder X-ray spectrum, observed by ASCA (Dotani et al. 1999) and *Chandra* ($\Gamma \sim 1.4$; see Stacey et al. 2011, which used the same *Chandra* observations presented here). The optical counterpart of 1E1339 was identified by Edmonds et al. (2004) as a star with a very blue $U-V$ colour, showing marked variability on timescales of hours.

1E1339 is the only supersoft X-ray source (SSS) identified in a Galactic GC, though three transient SSSs have been identified in M31 GCs (Henze et al. 2009, 2013), two of them clearly identified with nova explosions, which are the most frequent class of transient SSSs in M31 (e.g. Henze et al. 2011). The bright outburst and the supersoft spectrum suggest a physical connection to other galactic supersoft X-ray sources (SSSs). However, 1E1339's peak observed X-ray luminosity was ~ 100 times fainter than that of standard SSSs, suggesting a much smaller burning area.

The present work focuses on a systematic multiwavelength study of the faint X-ray sources in M3. The paper is organized as follows: in section 2, we report the *Chandra* and *HST* data we used in our studies. In section 3, we describe our analyses including data reduction, source detection, and the relevant techniques and methodologies used in astrometry, photometry, and counterpart identifications. In section 4, we discuss the possible nature of each X-ray source based on its photometric and spectroscopic properties. Finally, in section 5, we summarise our results.

Table 1. *Chandra* Observations

ObsID	Time of observation	Exposure time (ks)	Chip
4542	2003-11-11 16:33:18	9.93	ACIS-S
4543	2004-05-09 17:26:32	10.15	ACIS-S
4544	2005-01-10 08:54:31	9.44	ACIS-S

2 OBSERVATIONS

2.1 *Chandra* Observations

The globular cluster M3 was observed by the Advanced CCD Imaging Spectrometer (ACIS-S) on board the *Chandra X-ray Observatory*, using the *very faint* mode. Three observations, at roughly 6-month intervals, were taken, focused on monitoring 1E1339. A 1/2 subarray was used to reduce the frametime, and thus pileup from this relatively bright source, but the field of view still covers the whole half-light region of the cluster. Observation details are listed in Tab. 1.

2.2 *HST* Observations

We used *HST* WFC3/UVIS (GO12605, PI: Piotto), ACS/WFC (GO10775, PI: Sarajedini) and ACS/HRC and ACS/WFC (GO10008, PI: Grindlay) imaging data to search for possible optical counterparts. The WFC3 2012 data contained observations in the F275W (\sim UV), F336W (\sim NUV), and F438W (\sim B) filters, while the 2006 ACS data used the F606W (\sim V) and F814W (\sim I) filters. The ACS/HRC and ACS/WFC 2004 data were taken over a broad range of UV and optical bands, in conjunction with the second *Chandra* observation. This enables us to construct a simultaneous spectral energy distribution (SED) for the supersoft X-ray source 1E1339. Details of these observations are listed in Tab. 2.

3 ANALYSES

3.1 Merging *Chandra* Observations

The *Chandra* data were reduced using the *Chandra Interactive Analysis of Observations* software (CIAO) version 4.10¹ and CALDB version 4.7.8. We first reprocessed the data using the CIAO *chandra_repro* script to update the calibration, generating new level-2 event files. We then add the three observations to get a deeper view of the cluster. We first adjust aspect solutions between observations by using the brightest source 1E1339. The new aspect solutions were applied to the event files by using the CIAO *wcs_update* tool. Finally, the combined exposure map and the corresponding exposure-corrected image were generated by using the CIAO *merge_obs* tool. The resulting merged broad-band exposure-corrected (0.5 – 7 keV) X-ray image is shown in Fig. 1.

3.2 Source Detection

We generated an X-ray source list by running the CIAO *wavdetect*² tool on the combined broad-band X-ray image.

¹ <http://cxc.harvard.edu/ciao/>

² <http://cxc.harvard.edu/ciao/threads/wavdetect/>

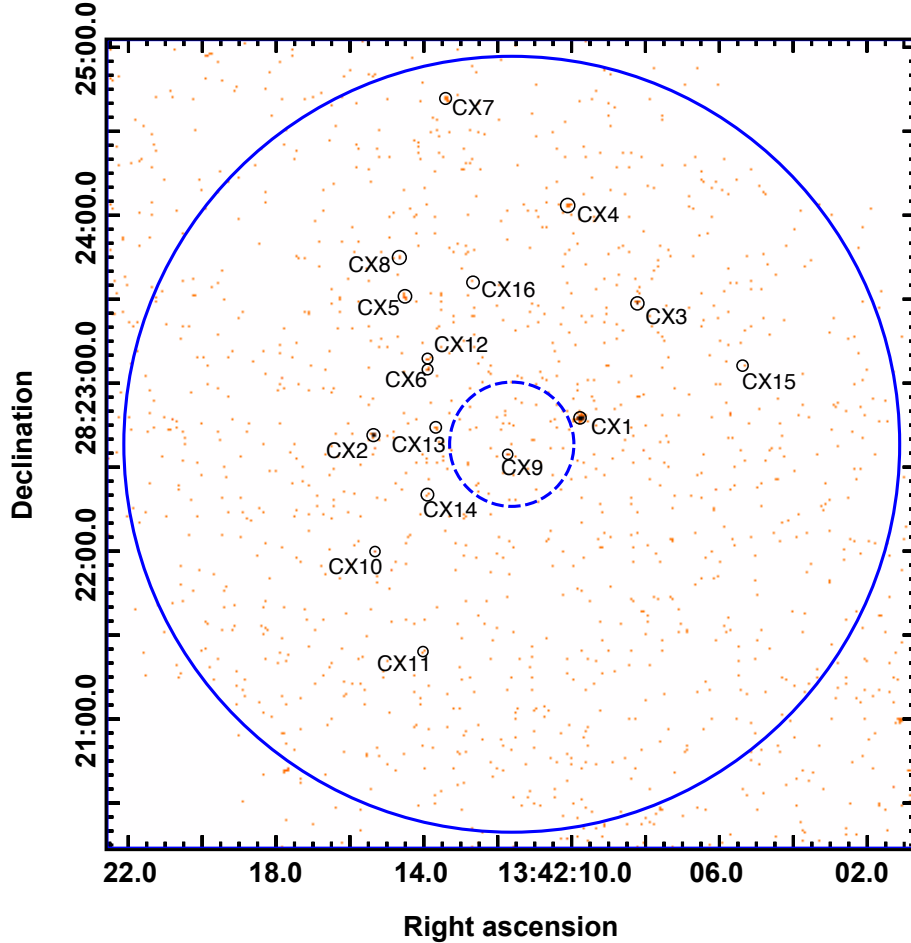


Figure 1. Merged 0.5 – 7 keV *Chandra* exposure-corrected ACIS-S X-ray image of the central 4.8×4.8 region of M3. The dashed blue circle shows the 0.37 core region; the solid blue circle shows the 2.31 half-light radius (Harris 1996, 2010 edition). Sources detected by *wavdetect* are marked with solid black circles. The size of each pixel is $0''.492$.

Table 2. *HST* Observations

GO	Time of observation	Exposure time (s)	Camera/Channel	Filter
10008	2004-05-09 17:51:18	620	ACS/HRC	F220W
	2004-05-09 17:41:19	464	ACS/HRC	F250W
	2004-05-09 17:17:33	1200	ACS/HRC	F330W
	2004-05-09 19:05:02	680	ACS/WFC	F435W
	2004-05-09 19:22:02	678	ACS/WFC	F555W
	2004-05-09 18:52:26	290	ACS/WFC	F814W
10775	2006-02-20 11:16:31	532	ACS/WFC	F606W ($\sim V$)
	2006-02-20 12:55:54	612	ACS/WFC	F814W ($\sim I$)
12605	2012-05-15 01:39:53	2490	WFC3/UVIS	F275W ($\sim UV$)
	2012-05-15 01:49:19	1400	WFC3/UVIS	F336W ($\sim NUV$)
	2012-05-15 01:36:38	168	WFC3/UVIS	F438W ($\sim B$)

The *wavdetect* algorithm correlates possible source pixels with a “Mexican Hat” function with different scale sizes and identifies pixels with sufficiently large positive correlation values to further calculate source positions, error circles and other information about the sources. We chose *scales* = 2, 4 to cover the possible sizes of point sources at different off-axis angles, and used *sigtthresh* = 3×10^{-6} (the reciprocal of the area of the region) to limit the expected number of false detections to 1. The detected sources are listed in Tab. 3. The right ascensions and declinations are the coordinates as

calculated by *wavdetect*. *Perr* is the 95% error circle following the empirical formula from Hong et al. (2005).

3.3 Source counts

We used the CIAO *srcflux*³ script to calculate the source counts in 3 energy bands: broad (0.5 – 7.0 keV), soft (0.5 –

³ <http://cxc.harvard.edu/ciao/threads/fluxes/>

Table 3. A catalogue of X-ray sources in M3.

Name	Positions ^a		Dist. ^b (")	P _{err} ^c (")	Net Counts (absorbed)			Notes
	α (J2000) (h : m : s)	δ (J2000) (deg : ' : '')			0.5 – 7.0 keV	0.5 – 2.0 keV counts (err) ^d	2.0 – 7.0 keV	
CX1	13:42:09.771	+28:22:47.618	25.8	0.295	1038.1 (32.3)	738.6 (27.2)	299.5 (17.4)	SSS (1E1339)
CX2	13:42:15.364	+28:22:41.458	49.5	0.321	138.4 (11.8)	137.5 (11.7)	1.0 (1.0)	qLMXB
CX3	13:42:08.218	+28:23:28.528	67.5	0.362	41.8 (6.5)	23.9 (4.9)	17.8 (4.2)	-
CX4	13:42:10.105	+28:24:03.498	87.6	0.410	19.8 (4.4)	10.0 (3.2)	9.8 (3.2)	-
CX5	13:42:14.511	+28:23:31.053	64.4	0.382	18.6 (4.5)	13.8 (3.7)	4.8 (2.2)	-
CX6	13:42:13.899	+28:23:04.927	40.2	0.403	16.0 (4.0)	3.0 (1.7)	13.0 (3.6)	CV
CX7	13:42:13.411	+28:24:41.737	125.8	0.519	8.8 (3.0)	5.0 (2.2)	3.9 (2.0)	CV/AGN
CX8	13:42:14.664	+28:23:44.921	78.7	0.482	7.9 (2.5)	4.9 (2.2)	2.9 (1.7)	CV?
CX9	13:42:11.730	+28:22:34.608	3.9	0.490	7.8 (2.8)	5.0 (2.2)	3.0 (1.7)	RS/AB
CX10	13:42:15.322	+28:21:59.867	62.1	0.539	7.0 (2.8)	3.0 (1.7)	4.0 (2.0)	-
CX11	13:42:14.023	+28:21:24.128	80.6	0.620	6.0 (2.6)	5.0 (2.2)	1.0 (1.0)	-
CX12	13:42:13.901	+28:23:08.819	42.9	0.498	5.8 (2.5)	6.0 (2.4)	0.0 (0.0)	CV/AGN
CX13	13:42:13.678	+28:22:44.243	27.8	0.453	5.8 (2.4)	4.9 (2.2)	1.0 (1.0)	CV/AGN
CX14	13:42:13.903	+28:22:20.201	35.1	0.543	4.9 (2.2)	3.9 (2.0)	1.0 (1.0)	AB?
CX15	13:42:05.389	+28:23:06.513	87.0	0.784	4.0 (2.0)	2.0 (1.4)	2.0 (1.4)	-
CX16	13:42:12.668	+28:23:36.034	59.4	0.534	3.9 (2.0)	3.0 (1.7)	1.0 (1.0)	CV/AGN

^a Coordinates from *wavdetect*^b Offsets from the center of the core in arcsec^c 95% error circles as calculated by Hong et al. (2005)^d errors generated by CIAO *srcflux* tool

2.0 keV), and hard (2.0 – 7.0 keV). The effective energy of each band was calculated as the flux-weighted average using the best-fit models of 1E1339 in Stacey et al. (2011). To calculate the combined counts, we first apply the script to each individual observation, and then add up the counts. For all sources except CX6 and CX12, the extraction region is defined by a circle that encloses 90% of the PSF at 1 keV, and the background region is an annulus with inner radius the same as that of the extraction region and outer radius 5 times the radius of the source region. Because CX6 and CX12 are close to one another, their background regions were defined separately as annuli excluding the other source. In Tab. 3, we ordered the sources in descending order of their observed counts in the broad band.

3.4 Optical Photometry

We used the wide-field observations from three epochs (2004, 2006, and 2012) to systematically study the photometry of this GC.

The 2012 WFC3/UVIS photometry has been analysed as part of the *Hubble Space Telescope UV Legacy Survey of Galactic Globular Clusters* (Piotti et al. 2015, GO-13297), and the reduced data and data products, including magnitudes of detected point sources, are now available to the public (Soto et al. 2017). However, we found that some stars detected on our images, which coincide with X-ray error circles, are not included in the Padova catalogue, though evidence for their presence is visible to the eye. Therefore, we also generated our own photometric catalogue by performing PSF-fitting photometry on the three WFC3/UVIS filters for counterpart searching. We used *HST* data products that are pipeline-processed, flat-fielded, and with charge transfer efficiency (CTE) trails removed (i.e., FLC images) to get the stacked images for photometry, absolute astrometry, and counterpart searches. We used the *HST* Drizzlepac

software version 2.0⁴ for image alignment and combination. For each filter, all FLC frames are first aligned to a reference frame (one of the FLC images) with the Drizzlepac *Tweakreg* tool. The aligned images were then combined using the Drizzlepac *AstroDrizzle* tool with *pixfrac*=1.0. In order to get higher resolution, the drizzle-combined images were oversampled by a factor of two so that their pixel size is half of the original (0.''02/pixel for WFC3/UVIS, and 0.''025/pixel for ACS/WFC). The drizzle-combined images of ACS/WFC were used for visual inspection of candidates and for making finding charts.

We then performed aperture and PSF-fitting photometry on the drizzle-combined WFC3 images (2012 observation) using the PyRAF⁵ DAOPHOT (Stetson 1987) package. A star list was first generated for each filter by the *daofind* task with 3σ detection threshold. We then chose relatively bright and isolated stars to model the PSFs. In order to account for possible spatial variability, at least 100 PSF candidate stars were selected across each image and the PSF model was set to be a second-order function of x and y (*varorder* = 2). The best-fit PSF model was then applied to all stars in the field by using *allstar*.

The following three steps were taken to calibrate the DAOPHOT/*allstar* photometry. First, magnitudes corresponding to a finite aperture were calibrated to those corresponding to an infinite aperture using the "curve of growth" method applied to a subset of reasonably isolated bright stars. Second, instrumental magnitudes of infinite aperture were shifted to the VEGAMAG system by using the WFC3 zeropoints from the STScI web page⁶. Finally, PSF-fitting photometry only gives relative magnitudes, so we cross-identified stars between aperture photometry and PSF-

⁴ http://www.stsci.edu/hst/HST_overview/drizzlepac⁵ http://www.stsci.edu/institute/software_hardware/pyraf⁶ http://www.stsci.edu/hst/wfc3/phot_zp_lbn

fitting photometry, and applied the average offsets to convert magnitudes in PSF photometry to instrumental magnitudes.

The photometry of the 2006 ACS/WFC observations (GO-10775, PI: Sarajedini) has been produced as part of the *ACS Globular Cluster Treasury Program* (Sarajedini et al. 2007; Anderson et al. 2008, GO-10775) which provides V₆₀₆ and I₈₁₄ magnitudes (available at the *Mikulski Archive for Space Telescopes* (MAST) website⁷).

We obtained photometry for the 2004 F435W (B) and F555W (V) images (GO-10008, PI: Grindlay) using software based on the program developed for the *ACS Globular Cluster Treasury Program*, described in Anderson et al. (2008) and known as Ksync. We performed photometric calibration to the VEGAMAG system by doing aperture photometry on moderately bright, isolated stars within a 0.15 arcsec radius aperture, finding the aperture correction to an infinite radius aperture from Sirianni et al. (2005), calculating the median offset between the Ksync photometry and the aperture photometry, and applying the calibrations from the HST calibration website.⁸.

With the obtained magnitudes for different filters, we constructed colour-magnitude diagrams (CMDs) by cross-matching catalogues in different filters. In Fig. 2 we show the resulting UV₂₇₅ – NUV₃₃₆, the NUV₃₃₆ – B₄₃₈, and the V₆₀₆ – I₈₁₄ CMDs; in Fig. 3, we show the B₄₃₅ – V₅₅₅ CMD.

3.5 Astrometry

The accuracy of *HST* astrometry is limited by at least two error sources. The first type of error comes from the fact that positions of guide stars used to derive the astrometric information are known with some uncertainties ($\lesssim 200$ mas for WFC3; $\lesssim 300$ mas for ACS. See ACS and WFC3 Handbooks; Lucas 2016, Deustua 2016). Secondly, errors are also introduced when the instrument aperture is mapped to the guide stars. The *Chandra* images are not astrometrized at the sub-arcsecond level, and therefore also require astrometric calibrations.

Our process of calibrating for astrometry includes two steps: 1. Calibrate one of the optical images to a known catalogue that has superior astrometry, and use this image as the reference frame; 2. Align other optical images to the reference frame, and align the *Chandra* catalogue to the reference frame for boresight correction—such that CX1 centres on its known counterpart (Edmonds et al. 2004). To fulfill this, we cross-matched source positions in one of our *daofind* catalogues with those from the Gaia Catalogue (Data Release 2; see Gaia Collaboration et al. 2016, 2018a). We chose the NUV₃₃₆ image as the reference image because it has a sufficiently long exposure, yet not so long to render bright sources saturated. We used a total of 895 Gaia sources that have relatively accurate positions (with errors in RA and DEC both ≤ 0.5 mas) found within a 1' search radius centred on the cluster core. Cross-matching resolved a total of 868 matches. We calculated the average offsets (Gaia – NUV₃₃₆) in RA and DEC, finding an average $\Delta\text{RA} \sim -0.384'' \pm 0.004''$ and an average $\Delta\text{DEC} \sim 0.254'' \pm 0.003''$ (1 σ errors). For

boresight correction, we found the Gaia – *Chandra* offsets of CX1 to be $\Delta\text{RA} \sim -0.22''$ and $\Delta\text{DEC} \sim 0.10''$.

3.6 Counterpart search

The principle of hunting for optical counterparts to XRBs more or less depends on the source class. For example, CVs typically have a strong UV excess that originates from the shock-heated region on the WD surface and/or the accretion disc, so they usually appear as blue outliers on UV – NUV or NUV – B CMDs. ABs are either K/M type main sequence stars (BY Draconis, or BY Dra) or F/K type subgiants (RS Canum Venaticorum or RS CVn). Examples of works using these classifications include Cohn et al. (2010) and Cool et al. (2013). Using these criteria, we searched possible counterparts primarily in the 95% error circles. If no interesting object was found within the 95% error circle, we also applied a somewhat larger searching region ($\leq 1.8P_{\text{err}}$), recognising that this procedure incurs a higher risk of spurious coincidences.

We also have to consider possible confusion from foreground stars and background AGNs. Foreground stars usually appear redder, while background AGNs appear bluer, than cluster members. To exclude non-members, we check the proper motion (PM) of each counterpart candidate and compare that with the PM of the GC. The cluster membership can be confirmed if the star moves in accordance with the cluster's systematic PM, and in disagreement with the PM of other possibilities. The enhanced angular resolution of HST cameras (e.g. ACS and WFC3) has made proper motion measurement possible over a relatively short span of time. Therefore, as part of the *Hubble Space Telescope UV Legacy Survey of Galactic Globular Clusters*, Piotto et al. (2015) includes a PM study of M3 by cross-matching the WFC3 source list with the ACS source list obtained 6.2 years earlier. Using the ACS(2006) and WFC3(2012) x and y positions from the Padova catalogue, we first calculated the displacements in x and y for each counterpart. The displacement can then be converted to proper motions with $v_i = \Delta x_i \times 50/\text{Epoch}$ (see Soto et al. 2017), where Epoch = 6.2 yr is the time interval between the ACS and the WFC3 observations. As another check on cluster membership, we incorporated the membership probability (P_μ) from the 2018 release of the public catalogue (see Nardiello et al. 2018).

We used stars that have at least one good photometric measurement in all three UV filters from the Padova catalogue as the sample for our PM check. We first computed PMs for each candidate counterpart and then compare them with the PM rms of the sample. A star is accepted as a cluster member if both its v_α and v_δ are smaller than 3 times the PM rms (≈ 1.779 mas yr⁻¹). Fig. 5 shows the PM distribution of the selected sample plotted in 4 separate magnitude bins, with candidate counterparts marked with red circles. The 3-rms limit of each bin is indicated with a dashed circle. Because the first bin is made of bright stars that are close to saturation, it has a relatively large rms. To exclude background AGN, we used the proper motion measurement of the cluster from GAIA DR2 (Gaia Collaboration et al. 2018b, see Table C.1.), from which we found $v_\alpha = 0.1127 \pm 0.0029$ mas yr⁻¹ and $v_\delta = 2.6274 \pm 0.0022$ mas yr⁻¹ for background AGN (marked with a red cross in Fig. 5).

⁷ <https://archive.stsci.edu/prepds/acsggct/>

⁸ <https://acszeropoints.stsci.edu/>

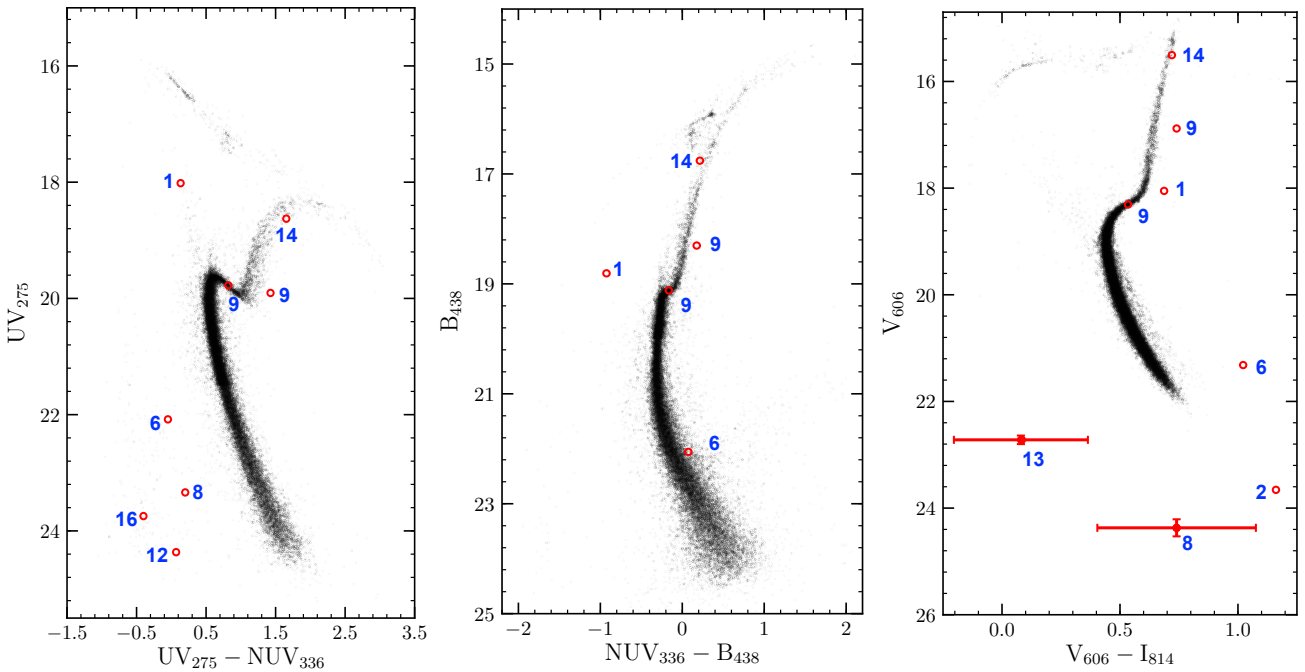


Figure 2. *Left:* $UV_{275} - NUV_{336}$ CMD generated by stars within a region of $140'' \times 140''$ centered on the cluster core. *Middle:* $UV_{336} - B_{438}$ CMD generated by stars within the same region. Both left and middle panels were generated using DAOPHOT results. *Right:* $V_{606} - I_{814}$ CMD from the catalogue of the *ACS Globular Cluster Treasury Program*. Optical counterparts are shown with red circles and annotated with their CX IDs (two potential counterparts are shown for CX9, though we find the brighter, redder one more likely). The error bars of CX8 and CX13 were indicated to show the uncertainty of their blue excesses.

Relying purely on photometric properties, we found potential counterparts to 10 of 16 *Chandra* sources. 8 of these are located within the corresponding 95% error circles, all except for the possible counterparts to CX7 and CX16. Fig. 4 shows a histogram of offsets for 10 identified counterparts in unit of their 95% error radii. PMs for our proposed counterparts to CX2, CX7, CX12, CX13 and CX16 are not available due to their nondetections in either 2006 or 2012, or both (see Tab. 4). However, the counterparts to CX1, CX6, CX8, CX9 and CX14 all have PMs less than 3 rms different from M3 (both in the α and δ directions), and are inconsistent with the expected location of AGN, outside the expected 3σ PM radius expected for background sources. The cluster memberships of the counterparts to CX1, CX6, CX9 and CX14 are confirmed by the calculated membership probability (P_μ). The counterpart to CX8 was detected as a very faint extension to a relatively bright star in the 2006 ACS/WFC observations (see Fig. 6), which might cause ambiguity in measuring the positions, so the PM information should be taken with care. Fig. 6 shows a mosaic of finding charts, wherein the most likely counterpart to each *Chandra* source is annotated with a red arrow. The corresponding optical colours and magnitudes of these stars are marked with red circles in Fig. 2. The magnitudes used for identification are summarised in Tab. 4.

3.7 Cluster Subpopulations and Chance Coincidences

In crowded regions (e.g. the cluster core), the chance of a potential counterpart being a coincidence is significant, so it is

important to estimate the number of chance coincidences for different cluster subpopulations. To get a census of cluster members, we used the PM information in the Padova catalogue to remove the non-members. We found ≈ 45554 cluster members detected in the WFC3 FOV. We applied polygonal selection areas on the UV - NUV CMD to divide members into different subpopulations (see Fig. 7). We found ≈ 2592 evolved stars, including ≈ 967 subgiants, and ≈ 1625 red giants. 108 stars were identified as (moderately) blue stars. Finally, we found a population of 169 blue stragglers and a population of only 9 red stragglers. The predicted number of chance coincidences per error circle was estimated by multiplying the number of stars in each subpopulation by the ratio of the average area of the error circles ($\approx 0.72 \text{ arcsec}^2$) to the WFC3 FOV. We found that the average error circle contains ≈ 1.25 normal cluster stars, though this varies somewhat by location in the cluster (see Fig. 6). Among evolved members, an average error circle contains ≈ 0.04 red giants and ≈ 0.03 subgiants, so there is a substantial chance of finding a giant and/or subgiant star within an error circle. However, the probability of finding a blue star in an error circle is quite small ($\approx 3.01 \times 10^{-3}$), as is the probability of a red straggler star ($\approx 2.47 \times 10^{-4}$) or a blue straggler star ($\approx 4.63 \times 10^{-3}$). Thus, the probability of finding a blue star in any of the 16 error circles by chance is only 5%, and that of finding a red straggler is only 0.4%. The probability of finding a blue straggler by chance coincidence is comparable to that of finding a blue star ($\approx 7\%$).

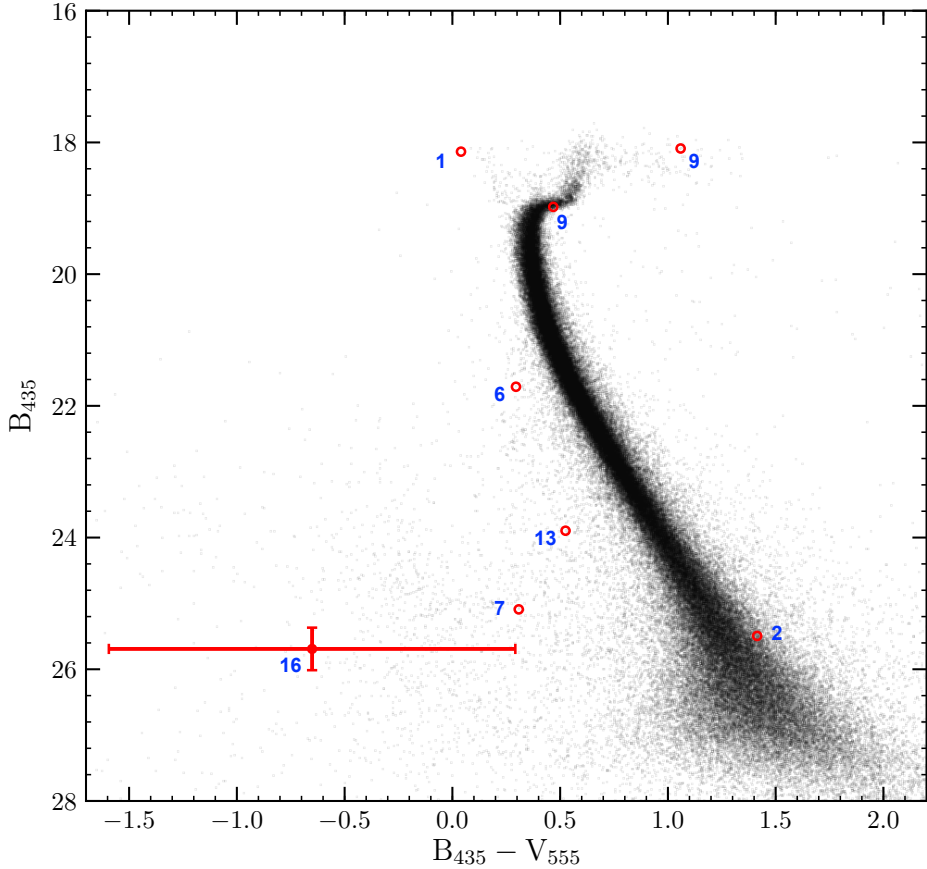


Figure 3. $B_{435} - V_{555}$ CMD from the 2004 ACS/WFC observation. Optical counterparts are annotated by red circles. The large photometric errors of CX16 are indicated with error bars.

Table 4. Magnitudes and colours of identified optical counterparts.

CX	Magnitudes ^a								Notes	
	2012			2006		2004				
	UV_{275}	NUV_{336}	B_{438}	V_{606}	I_{814}	B_{435}	V_{555}	P_μ^b		
1	18.02 ± 0.01	17.88 ± 0.02	18.81 ± 0.01	18.05 ± 0.03	17.37 ± 0.04	18.14 ± 0.18	18.10 ± 0.18	96.9%	Blue in UV, moderate red excess in V-I	
2	-	-	-	23.66 ± 0.03	22.50 ± 0.05	25.49 ± 0.48	24.08 ± 0.05	-	Faint MS star, small red excess	
6	22.08 ± 0.01	22.13 ± 0.02	22.06 ± 0.02	21.32 ± 0.02	20.30 ± 0.05	21.71 ± 0.22	21.42 ± 0.00	98.0%	Blue in UV, large red excess in V-I	
7 [†]	-	-	-	-	-	25.09 ± 0.33	24.78 ± 0.01	-	Faint blue star outside the error circle	
8	23.34 ± 0.03	23.14 ± 0.03	-	24.37 ± 0.16	23.63 ± 0.29	-	-	-	Faint blue star	
9	19.91 ± 0.02	18.48 ± 0.02	18.30 ± 0.01	16.88 ± 0.00	16.14 ± 0.00	18.09^*	17.03 ± 0.06	88.9%	Red straggler	
9	19.78 ± 0.02	18.96 ± 0.02	19.12 ± 0.02	18.31 ± 0.01	17.77 ± 0.01	18.98 ± 0.00	18.51 ± 0.00	97.7%	Subgiant	
12	24.37 ± 0.03	24.30 ± 0.04	-	-	-	-	-	-	Faint blue star, only detected in UV	
13	-	-	-	22.72 ± 0.08	22.64 ± 0.29	23.90^*	23.37 ± 0.72	-	Moderately blue star	
14	18.63 ± 0.02	16.97 ± 0.01	16.76 ± 0.01	15.51 ± 0.013	14.79 ± 0.04	-	-	96.6%	Red giant	
16 [†]	23.75 ± 0.02	24.15 ± 0.02	-	-	-	25.69 ± 0.32	26.34 ± 0.89	-	Faint blue star outside the error circle, only detected in UV	

^a Magnitudes are calibrated to VEGAMAG system

^b Probability of being a member of the cluster, from Nardiello et al. (2018)

* superscript indicates that the magnitude has a very large uncertainty and should be taken with care

[†] superscript indicates that the optical counterpart is outside the 95% Chandra error circle

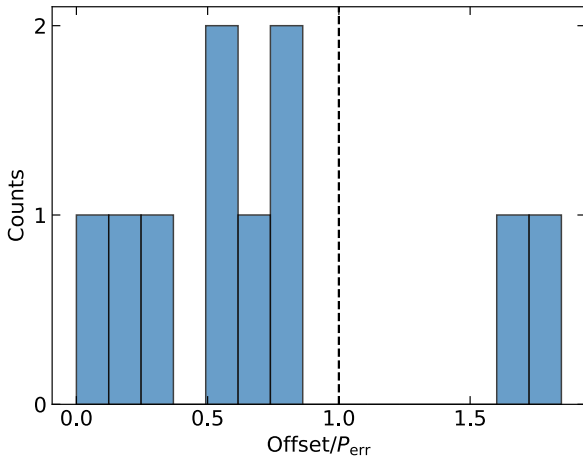


Figure 4. A histogram showing the distribution of offsets for the 10 identified counterparts. Each offset was normalised to the corresponding 95% error radius (P_{err}). The dashed line marks edges of the error circles.

CX	Filters				
	2012		2006		
	UV ₂₇₅	NUV ₃₃₆	B ₄₃₅	V ₆₀₆	I ₈₁₄
1	183.1	578.9	149.8	24.4	29.6
6	27.0	14.9	8.9	6.1	1.2
9	7.7	17.2	46.0	544.3	53.3
12	0.6	0.3	-	-	-
14	296.9	93.7	313.4	-	-
16	0.6	2.0	-	-	-

Table 5. Summary on resulting χ^2 from fitting constants to light curves in different filters.

3.8 Optical Variability

Signs of optical/UV variability can be helpful to further confirm the nature of the source, especially for CV identifications, since most CVs appear as blue variable stars (see e.g. Cool et al. 1998; Edmonds et al. 2003b; Dieball et al. 2017; Rivera Sandoval et al. 2018).

For the new counterparts that were detected in multiple exposures, we constructed *HST* light curves in the 2012 WFC3/UVIS and the 2006 ACS/WFC bands by doing DAOPHOT photometry (aperture photometry if the surrounding field of the counterpart is relatively uncrowded, e.g. CX16. Otherwise, PSF-fitting photometry was applied, e.g. CX9) on individual CR-removed, distortion-corrected FLC frames. The resulting light curves are shown in Fig. 8. We then used least-square fitting to fit each light curve to a constant and used the resulting reduced χ^2 (on Fig. 8) as a measure of variability. The resulting χ^2 are summarised in Tab. 5.

3.9 SED-Modelling of 1E1339

As mentioned above, the 2004 ACS data for 1E1339 (see Tab. 2) were taken over a broad range of filters, which yielded a dataset that can be used to construct and analyse the spectral energy distribution (SED). The target is well resolved and isolated in the three HRC filters, so that we can obtain photometric results with relatively high accu-

racy. However, the source is affected by saturation blemish from a nearby bright star on the B₄₃₅, V₅₅₅ and I₈₁₄ images. We, therefore, performed photometry with relatively small apertures (radius of 0.05'' or 1 ACS/WFC pixel) for these three filters. To calculate fluxes, we first calculated count rates from instrumental magnitudes. These count rates were then calibrated to infinite apertures by dividing the corresponding encircled energy (EE) fractions from Sirianni et al. (2005). Finally, count rates were converted to specific fluxes (F_λ) by multiplying the corresponding inverse sensitivities (PHOTFLAM⁹), i.e.

$$F_\lambda = \frac{\text{Count rate in a small aperture}}{\text{EE}} \times \text{PHOTFLAM}. \quad (1)$$

The specific fluxes in different filters are summarised in Tab. 6. The calibrated B₄₃₅ and V₅₅₅magnitudes are also summarised in Tab. 4.

We used tabulated stellar SED models from the Pickles library, an atlas of 131 stellar spectral models, (Pickles 1998) to model the SED. Spectra were convolved with the filter bandpasses and corrected for the expected extinction using PySynphot package¹⁰. The model spectra were then renormalised with a χ^2 minimization process (see Appendix). We first tried χ^2 fits with one-component models. The minimum of χ^2 was obtained with a type B5I spectrum, but still a bad fit ($\chi^2 \approx 153.89$). This was mainly caused by an obvious excess in the data (vs. the models) in the I₈₁₄ band ($\log(F_{\lambda,\text{data}}) - \log(F_{\lambda,\text{model}}) \approx 0.37$, corresponding to a difference in magnitude of ≈ 0.92), requiring a second cooler component to compensate for the excess. We, therefore, tried with two-component composite models. This is done by looping over all possible combinations of two components drawn from the Pickles library and picking out the combination with the smallest χ^2 . The best fit was obtained with a B2 + M0 model, which is a greatly improved fit ($\chi^2 \approx 3.42$). The M0 component now accounts for the V and I excesses relative to the B2 component. To constrain the spectral types of each component, we stepped one component at a time through different spectral types, allowing the other fit parameters to vary. We found a 90% confidence interval of K3-M2 or $T_{\text{eff}} = 3.75^{+1.05}_{-0.15} \times 10^3$ K for the redder component. For the bluer component, we found O8-B5 or $T_{\text{eff}} = 2.10^{+1.96}_{-0.58} \times 10^4$ K. The data overplotted with the best fit models are shown in Fig. 9.

Care should be taken, however, that the above spectral types do not necessarily reflect the actual traits of the accretor or the donor. Typically in CVs, the O or B type spectral components are ascribed to the combined light from the accretion disc and/or the WD surface, while the M type component might be caused by binary interactions. We will further discuss this in Sec. 4.1

3.10 X-ray spectral analysis

We performed detailed X-ray spectral analysis for sources with >100 counts that have not previously been published; only one source in our *Chandra* catalogue fits this description, CX2. For other sources with >10 counts, we perform

⁹ <http://www.stsci.edu/hst/acs/analysis/>

¹⁰ <http://pysynphot.readthedocs.io/en/latest/>

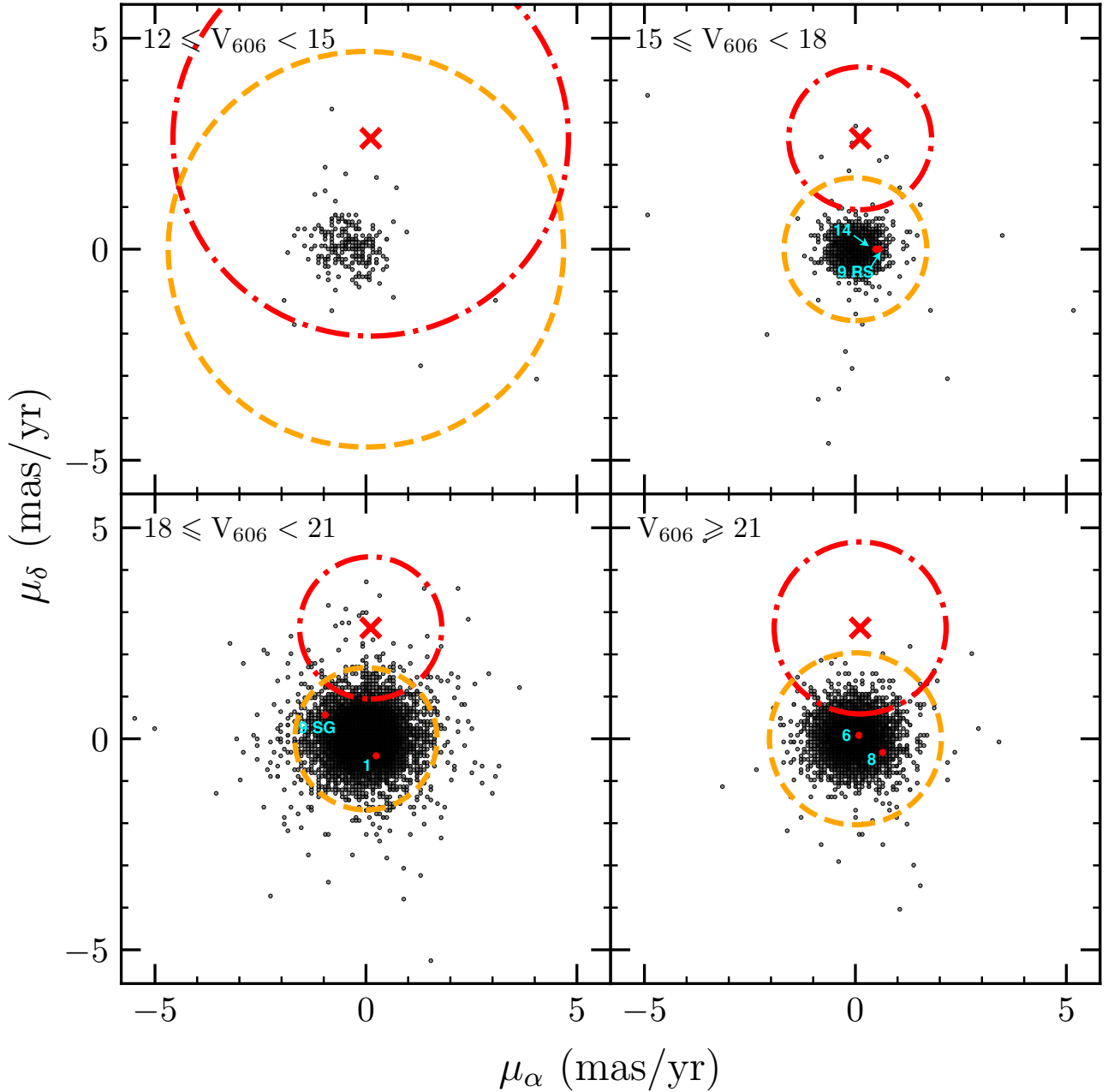


Figure 5. Proper motion distribution of stars with at least one good photometric measurement in each filter from the Padova Catalogue plotted in 4 V_{606} magnitude bins. The cluster's average proper motion corresponds to the zero point. The proper motion of background galaxies, obtained from GAIA DR2's estimate of the cluster motion, is marked with a red cross. Counterparts are shown with red points. The orange dashed circle in each panel shows the 3 rms radius within which stars are considered as likely cluster members. The red dotted-dashed circle in each panel shows the corresponding 3 σ composite error radius of the AGN proper motion.

Table 6. Calibrated specific fluxes (F_λ) of CX1 in different filters from the 2004 ACS observation.

Filters	ACS/HRC			ACS/WFC		
	F220W	F250W	F330W	F435W	F555W	F814W
Flux ($\times 10^{-16}$ erg s $^{-1}$ cm $^{-2}$ Å $^{-1}$)	6.62(43)	7.92(53)	7.36(50)	4.07(30)	2.83(14)	2.02(10)

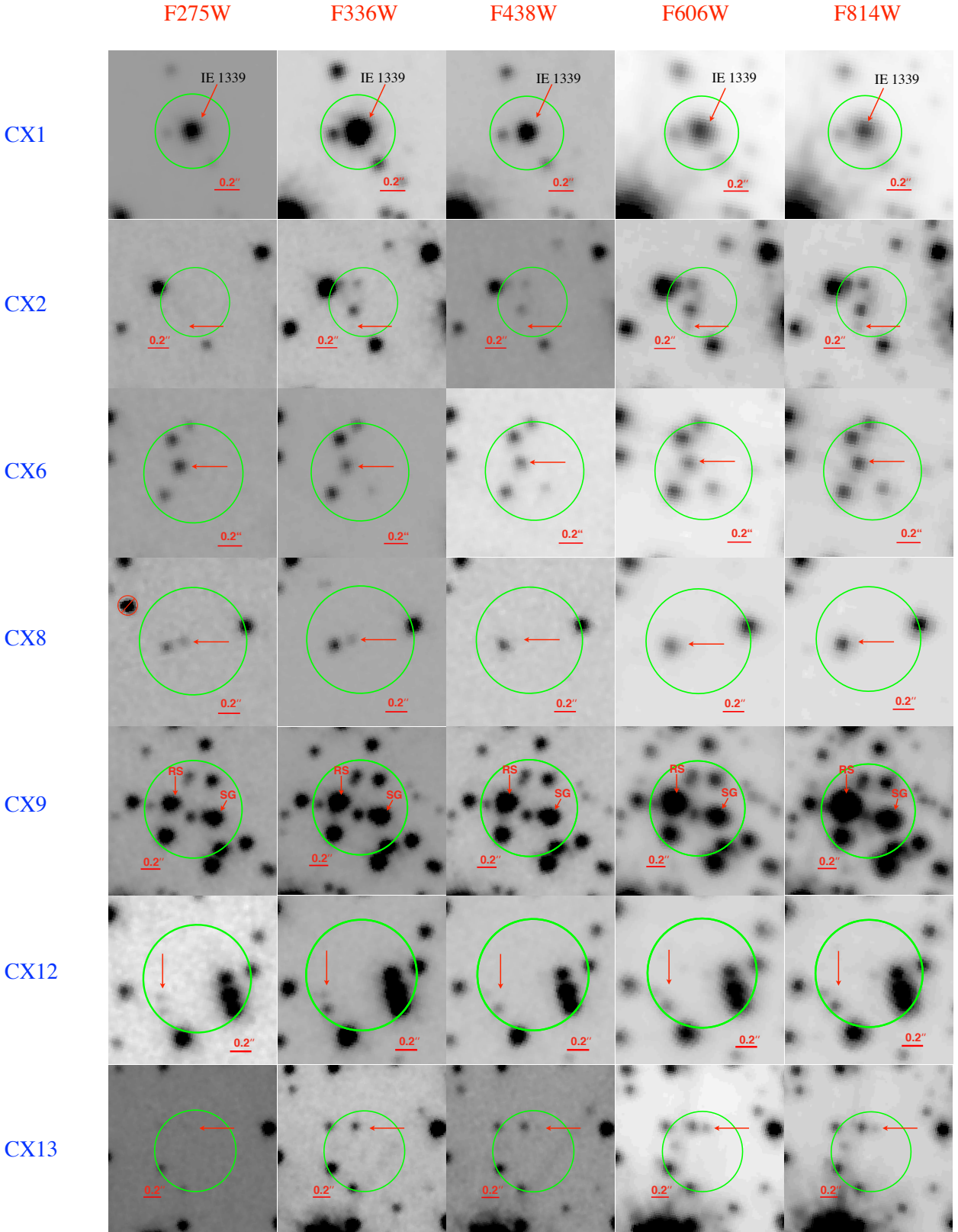


Figure 6. Finding charts for 7 identified optical counterparts in 5 different bands (UV bands are from the 2012 WFC3/UVIS observations; V₆₀₆ and I₈₁₄ bands are from the 2006 ACS/WFC observations) made from drizzle-combined images. North is up and east is to the left. The green solid circles represent the 95% *Chandra* error circles as calculated in Hong et al. (2005). Identified counterparts are annotated with red arrows. Note that the counterparts to CX12 was only found in the two UV filters (UV₂₇₅, NUV₃₃₆); similarly, the counterparts to CX2 and CX13 were only detected in the two ACS/WFC bands, so the red arrows on the other finding charts only point to their nominal positions. The counterpart to CX8 appears to be a faint extension in V₆₀₆ and I₈₁₄. Also, notice that a cosmic ray on the UV₂₇₅ finding chart of CX8 has been excluded to avoid confusion. The red straggler (RS) and subgiant (SG) potential counterparts to CX9 are annotated with arrows and texts.

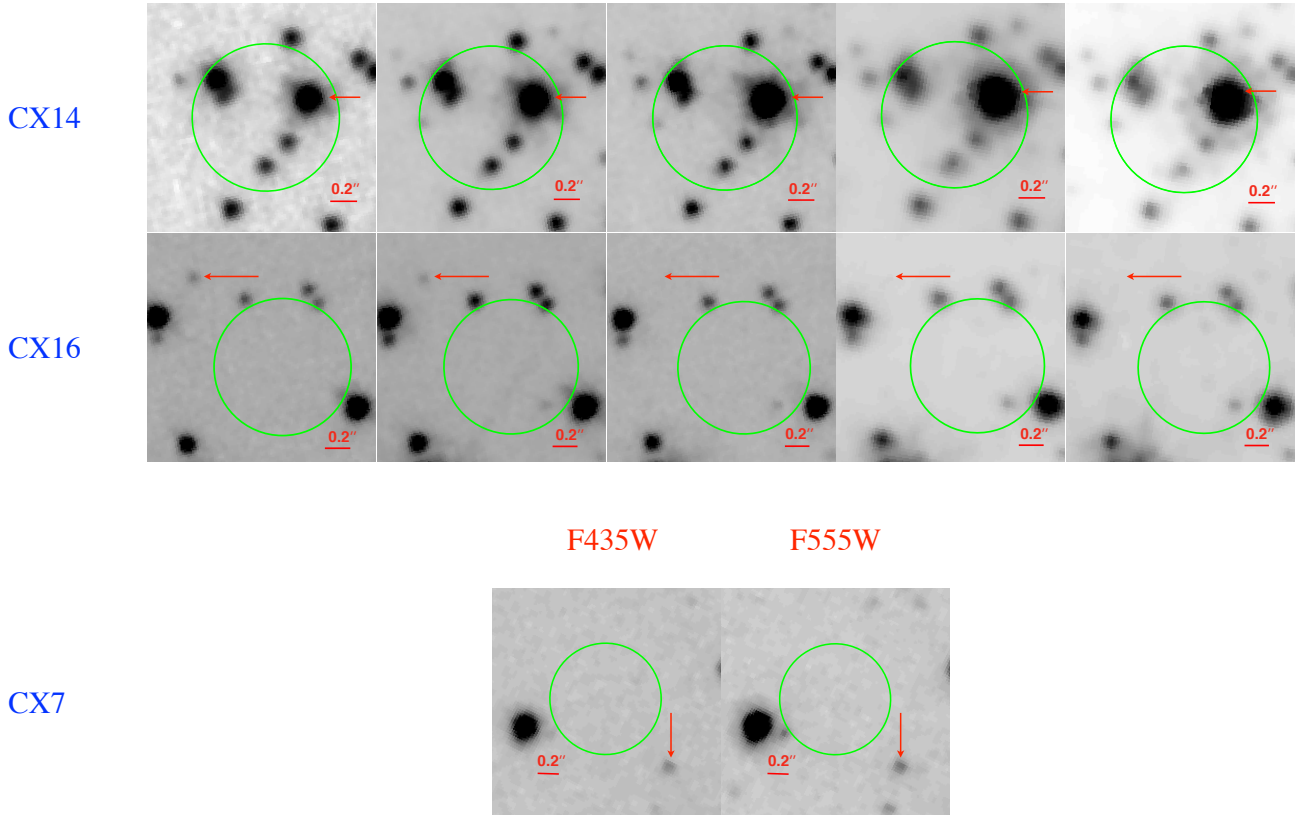


Figure 6 – continued CX7 was only covered by the 2004 ACS/WFC observations. Plausible counterparts for CX7 and CX16 lie somewhat outside the 95% *Chandra* error circle.

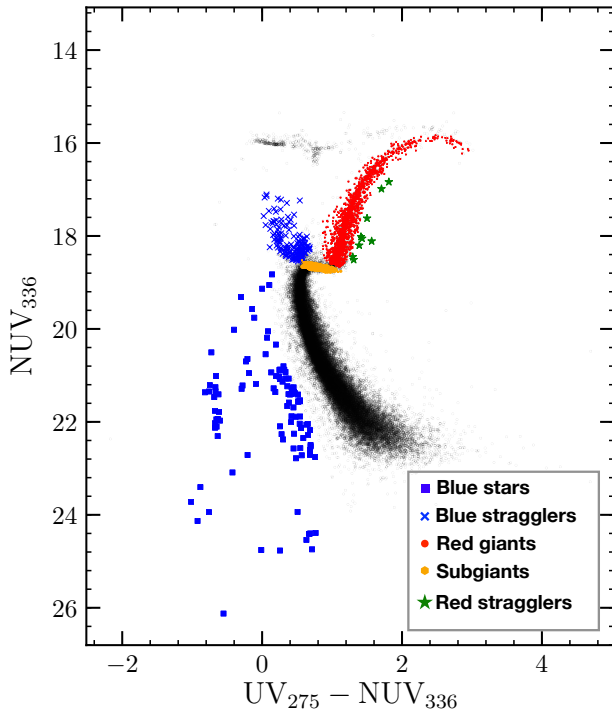


Figure 7. Proper motion cleaned $UV_{275} - NUV_{336}$ CMD overplotted with different subpopulations.

simplified spectral analyses. We used the CIAO *specextract*¹¹ script to extract spectra of these sources from each of the 3 observations. Because these observations do not span a very long time, to get better statistics, we combined the 3 spectra and their responses using FTTOOLS/ADDSPEC¹² before doing the analysis. The combined spectra were then re-binned using the CIAO *dmggroup*¹³ tool to at least 1 count per bin. Spectral analysis was then performed on the combined spectra with HEASoft/Xspec version 12.9.1 using C-statistics (Cash 1979). Because the accuracy of the *Chandra* response matrix file falls off at low energies, we ignored energy channels below 0.5 keV during the fits. (These channels are included in the plots just to demonstrate the obvious excess at low energies.) We fixed the absorption hydrogen column density at the cluster value $\sim 8.7 \times 10^{19} \text{ cm}^{-2}$, which is derived by applying the conversion factor ($\sim 2.81 \pm 0.13 \times 10^{21}$) from Bahramian et al. (2015) and using $E(B-V) = 0.01$ from Harris (1996, 2010 edition).

We tried fits to CX2 with multiple models including an empirical power law (POWERLAW), a blackbody (BBODYRAD), a neutron star atmosphere (NSATMOS), and a hot plasma model (VMEKAL). For sources with more than 10 counts but fainter than CX2, we fit an individual power law to each source. We combined the spectra of

¹¹ <http://cxc.cfa.harvard.edu/ciao/threads/pointlike/>

¹² <https://heasarc.gsfc.nasa.gov/ftools/caldb/help/addspec.txt>

¹³ <http://cxc.harvard.edu/ciao/ahelp/dmgroup.html>

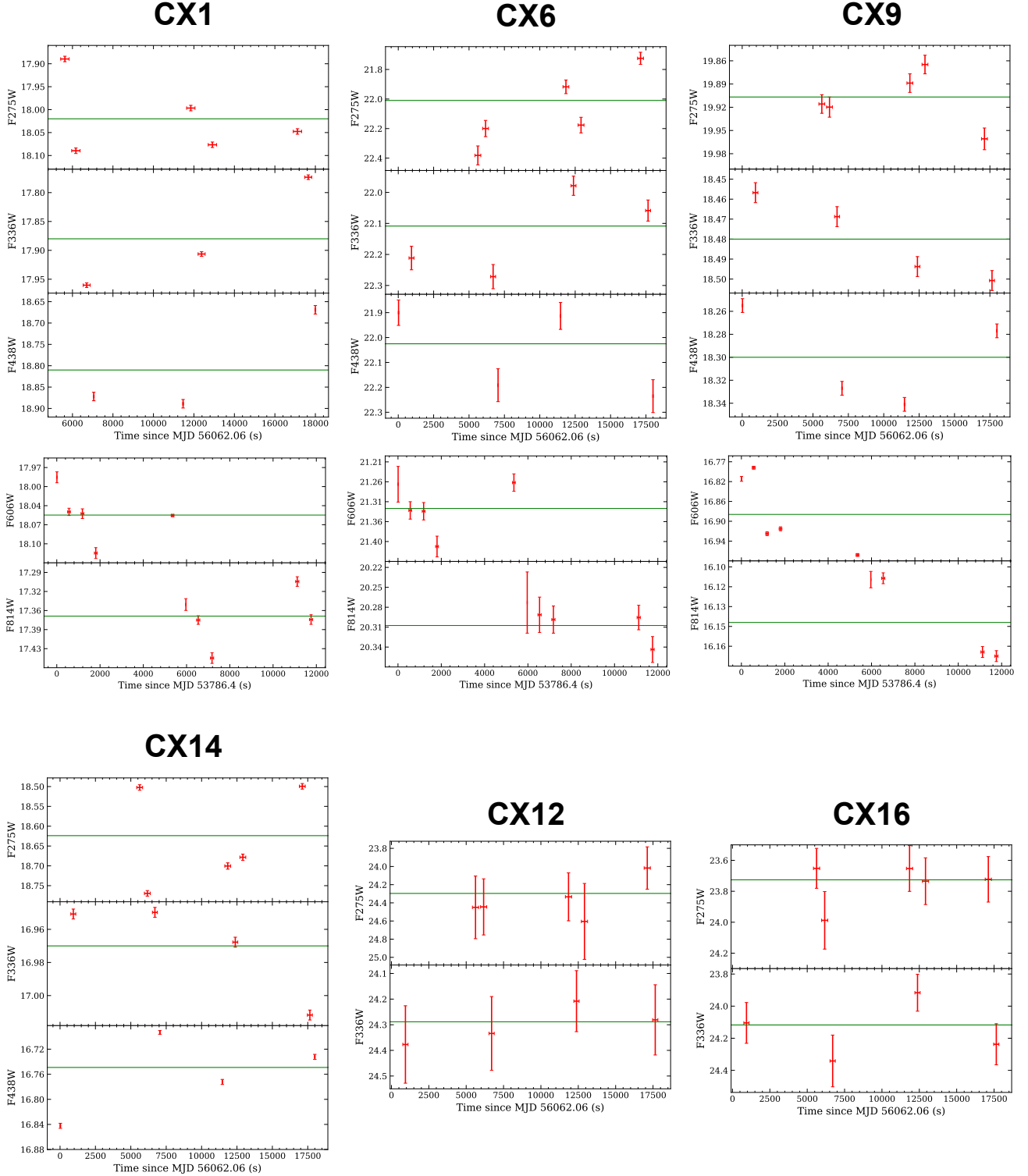


Figure 8. Optical/UV light curves of the identified counterparts that have detections in multiple exposures in the WFC3/UVIS observations (2012) and/or the ACS/WFC observations (2006). Photometric errors are from DAOPHOT software. The best fit constants are indicated with a solid green line.

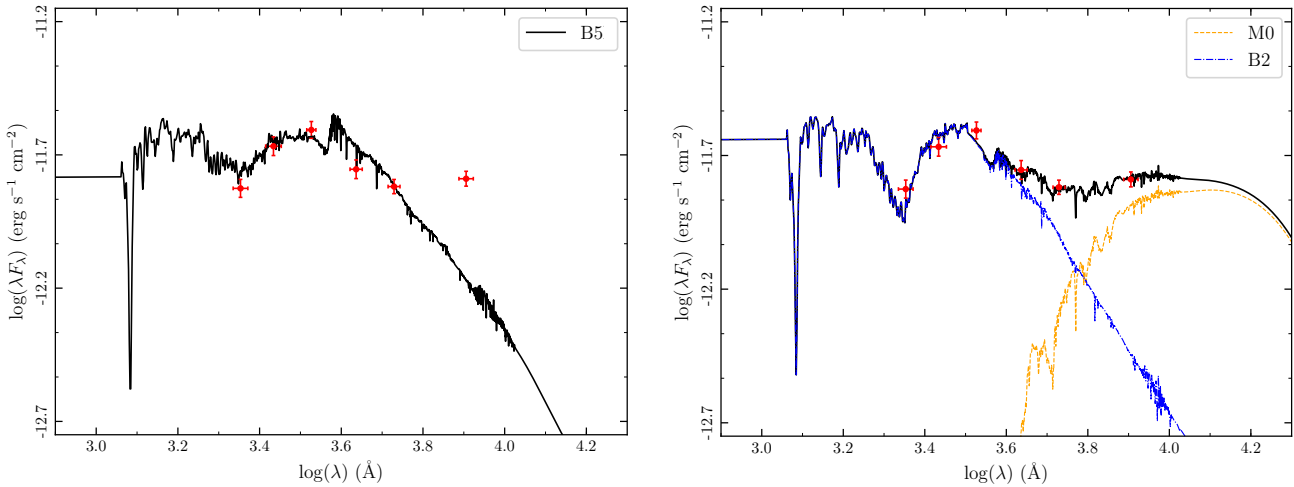


Figure 9. Best fit SED models and data from the 2004 observations. *Left panel* shows the best fit single-component model (solid black) overplotted with the data (red). *Right panel* shows the same data (red) and the best fit two-component model (solid black), composed of a renormalised B2 component (blue dashed-dotted) and an renormalised M0 component (orange dashed).

sources with less than 10 counts (CX7-CX16) and fit a power law to the combined spectrum to get an average photon index. We obtained an average index of $\Gamma \approx 1.3$, which was then applied to the spectra of CX7-CX16 to calculate fluxes (fluxes of sources fainter than CX9 were calculated with *srfclux*, so no C-statistic or goodness calculation is available). All fitting results are summarised in Tab. 7.

4 INDIVIDUAL SOURCES & DISCUSSIONS

4.1 CX1/1E1339

The optical counterpart of 1E1339 was first identified by Edmonds et al. (2004), using WFPC2 data, to be a star with a very blue U – V colour (but lying on the subgiant branch in a V – I CMD), showing marked variability on timescales of hours. Our photometry confirms its blue U – V excess. Though 1E1339 lies on the blue straggler region in UV-NUV and B – V CMDs, it does not lie in the blue straggler region in other CMDs (see Figures 2, 3). This illustrates that multiple emission components are required, as expected in cataclysmic variables; examples of real blue straggler counterparts, and another CV that only appears to lie on the blue straggler sequence in some CMDs, can be found in Edmonds et al. (2003a). The ACS photometry from the *ACS Globular Cluster Treasury Program* revealed a red excess in V – I colour ($E(V-I) \approx 0.09$ with respect to the red giant branch), suggesting a red straggler (RS) secondary (Mathieu et al. 2003; Geller et al. 2017). Unusually red secondaries in XRBs have been observed in some CVs in 47 Tuc (Edmonds et al. 2003a), M30 (Lugger et al. 2007), and NGC 6752 (Thomson et al. 2012). Such bloating may be due to irradiation, or more likely due to continued mass loss from the donor, as expected under standard CV evolutionary theory (Knigge et al. 2011). Using the correspondences between T_{eff} and V – I colours from Cox (2000), we found that the envelope of 1E1339’s companion should have expanded by roughly 3% in order to have the observed red excess. Leiner et al. (2017) and Ivanova et al. (2017) show evolutionary models

for binary mass-transferring systems that indeed demonstrate optical colours like these. This star also varies by ≈ 0.2 mags in the UV and B filters on timescales of hours. Fitting its lightcurves to a constant gives a poor reduced χ^2 (e.g. reduced $\chi^2 \approx 183$ for the UV_{275} filter, see Fig. 8).

Our SED fitting result corroborates this observed red excess (≈ 0.92 mags as mentioned in Sec. 3.9), since a second, cooler component is required to get a satisfactory fit. The red excess might be partly due to variability, either long term or short term, of CX1. However, the presence of this red excess in two independent *HST* epochs (2004 and 2006 V – I CMDs) indicates its extreme colour is likely real. The 0.92-mag difference between the observed and expected I magnitudes is larger than can reasonably be explained by the observed short-term variability, of typically 0.2 magnitudes (Edmonds et al. 2004).

The cooler spectral component suggests an M0-type subgiant, while the bluer component has a spectral type for a B2-type giant, which is likely to represent the combined light from the WD and the accretion disc. We note that the extreme UV brightness indicates a high rate of mass transfer through the accretion disc. Should the accretor be a neutron star or black hole, a very high X-ray luminosity ($> 10^{36}$ erg/s) would be expected; the lack of such bright X-rays indicates that the accretor is almost certainly a white dwarf.

4.2 CX2— a quiescent low-mass X-ray binary (qLMXB)?

To model CX2’s X-ray spectrum, we first tried a simple absorbed power-law model (TBabs*POWERLAW) and found a rather soft photon index ($\Gamma = 3.6^{+0.4}_{-0.3}$). The soft nature of this source was further confirmed by the low kT (≈ 0.2 keV) from a blackbody fit (TBabs*BBODYRAD). We then tried fits with more physically motivated models. A thermal plasma fit (TBabs*VMEKAL) yielded a slightly worse fit (Goodness = 92.9%) with a $kT \sim 0.4$ keV. A neutron star atmosphere model (TBabs*NSATMOS, Heinke et al. 2006) consistently yielded a low $kT_{\text{eff}} \approx 0.10$ keV (typical for

Table 7. Summary of X-ray spectral analyses.

Source CX	Model	n_H^a (10^{19} cm $^{-2}$)	Γ or R_i^b	kT (keV)	$f_{0.5-7.0, \text{unabs}}$ (10^{-16} erg cm $^{-2}$ s $^{-1}$)	$L_{0.5-7.0, \text{unabs}}$ (10^{30} erg s $^{-1}$)	Cstat/dof	Goodness
2	TBabs*POWERLAW	(8.7)	$3.6^{+0.4}_{-0.3}$	-	$206.6^{+30.1}_{-25.4}$	$257.2^{+37.5}_{-32.2}$	53.1/59	66.8%
	TBabs*BBODYRAD		$1.4^{+0.3}_{-0.3}$	$0.20^{+0.02}_{-0.02}$	$177.4^{+25.9}_{-23.2}$	$220.9^{+32.2}_{-29.4}$	49.3/59	53.8%
	TBabs*VMEKAL		-	$0.42^{+0.11}_{-0.06}$	$184.1^{+26.8}_{-24.5}$	$229.2^{+33.4}_{-30.5}$	60.4/59	92.9%
	TBabs*NSATMOS		$8.6^{+5.7}_{-5.8}{}^*$	$0.10^{+0.06}_{-0.02}$	$183.3^{+38.1}_{-24.4}$	$228.2^{+35.5}_{-30.3}$	46.2/59	9.6%
3			$0.8^{+0.4}_{-0.4}$		$167.5^{+45.0}_{-38.1}$	$208.6^{+36.1}_{-37.5}$	43.1/34	51.9%
4	TBabs*POWERLAW	(8.7)	$0.8^{+0.6}_{-0.8}$	-	$63.9^{+27.3}_{-21.4}$	$79.5^{+34.0}_{-26.6}$	11.08/15	3.3%
5			$2.1^{+0.8}_{-0.7}$		$43.3^{+21.6}_{-13.8}$	$53.9^{+21.9}_{-16.2}$	21.6/17	29.2%
6		(6×10^3)	$-0.7^{+0.7}_{-0.8}$		$104.9^{+50.2}_{-38.8}$	$130.6^{+62.4}_{-47.3}$	18.1/13	6.7%
7			$1.2^{+1.2}_{-1.3}$		$191.2^{+93.0}_{-70.4}$	$238.1^{+155.7}_{-87.7}$	20.1/13	25.8%
8					$41.7^{+22.2}_{-16.5}$	$52.0^{+27.7}_{-29.3}$	10.7/15	66.9%
9					$27.5^{+13.3}_{-16.8}$	$34.2^{+21.7}_{-16.6}$	3.4/7	33.1%
10					$20.0^{+16.8}_{-11.9}$	$24.9^{+21.0}_{-17.7}$	1.0/6	8.5%
11	TBABS*POWERLAW	(8.7)	$1.3^{+0.4}_{-0.4}$	-	$17.0^{+8.1}_{-7.3}$	$21.1^{+20.5}_{-10.5}$	-	-
12			$14.8^{+8.1}_{-7.6}$		$18.4^{+21.0}_{-9.5}$	-	-	-
13			$15.9^{+16.8}_{-7.5}$		$19.8^{+20.9}_{-9.4}$	-	-	-
14			$13.3^{+16.2}_{-7.5}$		$16.5^{+20.2}_{-8.4}$	-	-	-
15			$11.0^{+7.1}_{-6.9}$		$13.6^{+15.0}_{-8.6}$	-	-	-
16			$10.5^{+13.5}_{-6.2}$		$13.0^{+16.7}_{-7.7}$	-	-	-

^a Values in the parentheses indicates that the parameter is fixed during the fit

^b R_i is the radius of the emission region for BBODYRAD model, or the neutron star radius for the NSATMOS model, both in km

* indicates that the error extends beyond the hard limit

a quiescent low-mass X-ray binary (qLMXB) with an NS radius $R_{\text{NS}} \approx 8.6$ km (Goodness = 9.6%), or $kT_{\text{eff}} \approx 0.09$ when R_{NS} was frozen to 10 km (Goodness = 13.2%). The models and best fit parameters are summarised in Tab. 7. Fig. 10 shows the spectrum overplotted with the best fit models (see Tab. 7). Below 0.5 keV, the data are poor fits, but we attribute this to the difficulty of calibrating this portion of the X-ray spectrum.

We identify a potential optical counterpart to this source, a star that lies on the red side of the main sequence in the B₄₃₅ – V₅₅₅ CMD (Fig. 3). This star shows a relatively large photometric error in the B₄₃₅ band (see Tab. 4), which makes its CMD position uncertain. However, as this counterpart is not clearly off the main sequence, Sec. 3.6 suggests that this star may well be a chance coincidence.

We consider several possible natures for CX2; quiescent LMXB, MSP, CV, or AB in the cluster, or a background or foreground source. The NS atmosphere fit is consistent with a qLMXB nature, with a radius consistent with emission from a full NS surface. However, it is inconsistent with the expectation of emission from NS polar caps as seen in typical MSPs (Zavlin et al. 2002; Bogdanov et al. 2006). Although the VMEKAL fit is statistically reasonable, the implied temperature is low. If CX2 is a member of M3, its X-ray luminosity of 2×10^{32} erg/s is at the very high end of X-ray luminosities for globular cluster CVs, and all known CVs in globular clusters with $L_X > 10^{31}$ erg/s have much harder X-ray spectra (e.g. Heinke et al. 2005b; Poonley & Hut 2006), so a CV nature can be ruled out empirically. Verbunt et al. (2008) showed that nearby chromospherically active stars are limited in their X-ray luminosity, with $\log L_X < 32.3 - 0.27 M_V$, while active binaries in globular clusters are limited by $\log L_X < 34.0 - 0.4 M_V$ (Bassa et al. 2004). CX2’s suggested counterpart has $M_V = 8.6$ (Tab. 4) and $L_X = 2 \times 10^{32}$ erg/s (Tab. 7), so CX2 lies well above both limits (see Fig. 11), strongly suggesting that it is not an AB. If CX2 were instead a foreground AB, the optical counterpart to CX2 should be brighter than $M_V = -0.3$; however, no bright cluster non-members were found within

the error circle of CX2, arguing against a foreground system. A bright cluster MS star ($P_\mu = 98.1\%$) is located NW of the error circle (Fig. 6), but is still too faint (by 0.6 mags, $V \approx 19.7 \pm 0.03$; see Fig. 11). Furthermore, X-ray bright cluster ABs generally have harder X-ray spectra than fainter ones (e.g. Heinke et al. 2005b), which contradicts the soft nature of the source. We therefore conclude that CX2 is most likely to be a qLMXB.

Considering the relatively low central density and large mass of M3, it is interesting to consider whether this quiescent LMXB is more likely to be generated from a primordial binary (that is, via a similar evolutionary path as similar objects outside clusters), or via dynamical encounters (as the majority of quiescent LMXBs and millisecond pulsars in GCs are thought to be produced). To calculate the probability of this quiescent LMXB being a primordial binary, we use estimates of the total number of quiescent neutron star LMXBs in the Milky Way, which center around 10^3 to 10^4 systems (Pfahl et al. 2003; Kiel & Hurley 2006; Jonker et al. 2011; Britt et al. 2014, Heinke et al. 2018, in prep.). We use the Milky Way’s stellar mass of $5 \times 10^{10} M_\odot$ (Cox 2000), and an estimate of M3’s stellar mass of $6 \times 10^5 M_\odot$ (adjusting the calculations of Gnedin et al. 2002¹⁴ to use the average mass-to-light ratio of 1.86 from Watkins et al. 2015), to predict 0.01 to 0.1 quiescent LMXBs in M3. Some population syntheses (e.g. Pfahl et al. 2003) do generate up to 10^5 LMXBs in the current Milky Way, which would predict of order 1 quiescent LMXB in M3. However, such a large number of quiescent LMXBs, in a Galaxy with of order 100 persistently bright LMXBs, is strongly empirically disfavored by the observed ratio of $\sim 10\text{--}20$ quiescent LMXBs per persistently bright LMXB in globular clusters (Heinke et al. 2003, 2005a), and by the other empirical estimates cited above. From the dynamical side, 5 quiescent LMXBs are observed in 47 Tuc (Heinke et al. 2005a), and M3 has a stellar interaction rate 19% that of 47 Tuc (Bahramian et al. 2013), so 0.97

¹⁴ <http://www-personal.umich.edu/~ognedin/gc/vesc.dat>

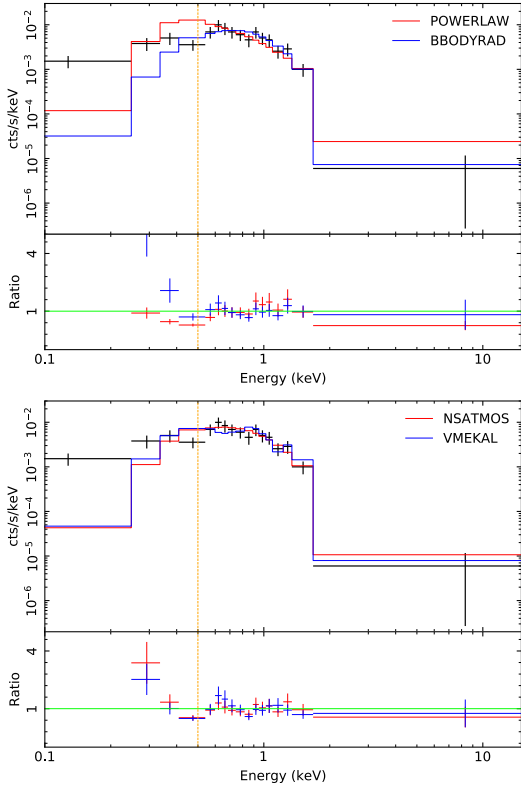


Figure 10. *Chandra* spectra of CX2. The top panel shows the rebinned (only for plotting purpose) data (black) with the best fit POWERLAW model and BBODYRAD model overplotted with a solid red line and a solid blue line, respectively. The bottom panel shows the same data, but overplotted with the best fit VMEKAL model (blue) and NSATMOS model (red). The yellow dashed line indicates the energy limit at 0.5 keV, below which channels were ignored during the fits. Ratio = data/model.

dynamically-formed quiescent LMXBs are predicted in M3. Thus, we find it 10–100 times more likely that this quiescent LMXB was formed dynamically, rather than primordially.

As a point of interest, performing the same calculation for the quiescent LMXB in ω Centauri (Rutledge et al. 2002) indicates a prediction of 0.04–0.4 primordial systems, vs. 0.45 dynamically formed systems, suggesting that the ω Centauri quiescent LMXB has a decent chance to be a primordial system.

4.3 CX6

A power-law fit to CX6’s X-ray spectrum produces a negative photon index ($\Gamma = -0.7^{+0.8}_{-0.7}$) if we freeze the n_H at the cluster value. However, Γ becomes more physically reasonable when N_H is allowed to float to a higher value. For example, at $N_H = 6.0 \times 10^{22} \text{ cm}^{-2}$, $\Gamma = 1.2^{+1.1}_{-1.3}$.

The optical counterpart to this source is very blue in UV colours ($E(UV - NUV) \approx -0.85$), but the $V - I$ colour indicates a very large red excess in visible light, $E(V - I) \approx 0.37$, compared to the main sequence. This red excess was confirmed in the 2004 ACS/WFC $V_{555} - I_{814}$ CMD (see Fig. 12) with $E(V - I) \approx 0.43$ with respect to the MS; however, using the B_{435} and V_{555} magnitudes from the same epoch, the star shows moderate blue excess relative to the MS (see

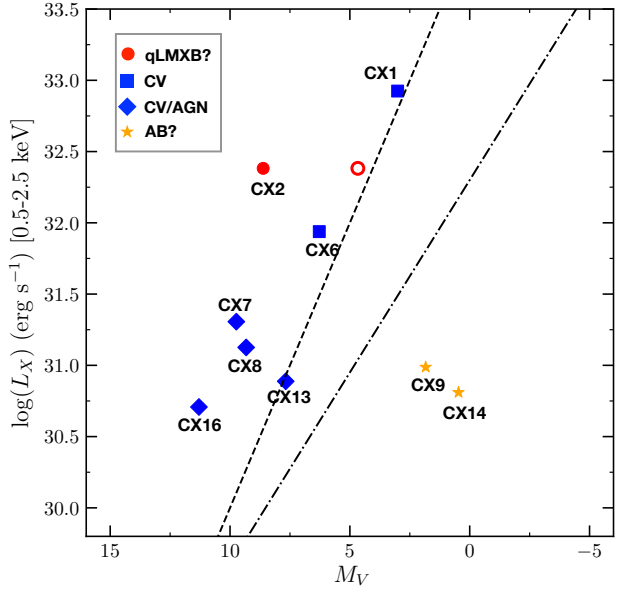


Figure 11. 0.5 – 2.5 keV L_X vs. absolute V band magnitudes (using V_{555} for CX7 and CX16, and V_{606} for others). L_X of CX1 is from Stacey et al. (2011). The dashed line corresponds to the $L_X = 34.0 - 0.4M_V$ separatrix from Bassa et al. (2004), dividing cluster CVs and ABs. The dotted-dashed line corresponds to the $L_X = 32.3 - 0.27M_V$ separatrix from Verbunt et al. (2008), marking the upper limit of L_X for nearby ABs. CV candidates with confirmed cluster memberships are marked with filled blue squares. Possible CV/AGN candidates are marked with filled blue diamonds. The red filled circle marks the location of CX2 if we were to adopt the suggested counterpart. For comparison, the red open circle indicates the location of CX2 on the plot if we adopt the bright MS star mentioned in Sec. 4.2 as the counterpart.

Fig. 3). Assuming the same V magnitude as CX6, the $V - I$ colour on the main sequence ($V - I \approx 0.65$) corresponds to an F9V-G0V dwarf with $T_{\text{eff}} \approx 5900$ K, whereas CX6 corresponds to a K3V-K3.5V dwarf with $T_{\text{eff}} \approx 4800$ K (spectral types and T_{eff} ’s are from Pecaut & Mamajek 2013). Again, if we apply the “bloated envelope” scenario as for CX1, the change in T_{eff} requires that the companion to be bloated by a factor of ~ 1.5 , which does not seem physically reasonable. Although high measured N_H ’s are common among AGNs, both CX6’s PM and the associated P_{μ} strongly support its cluster membership. In Sec. 3.6, we estimated the number of chance coincidences of blue stars to be minuscule ($\approx 2.14 \times 10^{-3}$), so the suggested counterpart is very unlikely to be spurious. Therefore, the high N_H might imply a CV seen edge-on, such as the CVs W8, W15, and AKO9 in 47 Tuc (Heinke et al. 2005b), but the red excess remains unexplained. Optical/UV variability analyses indicate strong UV and B variabilities to this star, suggestive of a CV nature, which might also be the cause of the observed simultaneous blue and red excess. Future spectroscopic study (e.g. with integral field units, such as MUSE) of this object could determine its nature.

4.4 CX8, CX12 and CX16

Similar to CX1 and CX6, the counterparts to these sources also show obvious UV excesses. Considering the calculations

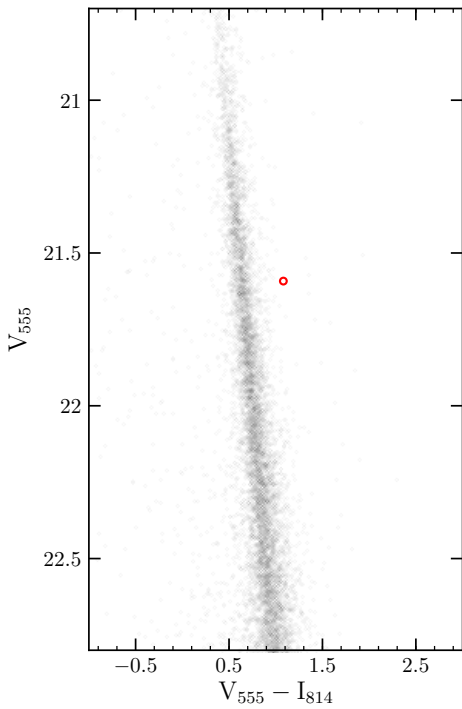


Figure 12. $V_{555} - I_{814}$ CMD from the 2004 ACS/WFC observations. The red circle marks the location of the CX6 counterpart.

of Sec. 3.7, none of these counterparts are likely to be chance coincidences, so they should be CVs or background AGNs. The 2012 WFC3 observations only detected these three counterparts in the two UV bands (UV_{275} and NUV_{336}). However, the 2004 ACS observations detected the counterpart to CX16, which shows a blue excess in the $B_{435} - V_{555}$ CMD with a relatively larger error bar (see Fig. 3). Although CX8 is apparently detected in the ACS GC survey catalogue (and therefore has a measured PM), this detection appears as a faint extension to a nearby bright star, which results in a larger photometric error and makes the blue excess more uncertain. Identifications of the faint optical counterparts to CX12 and CX16 are even more difficult, due to the lack of both accurate $V - I$ colours, and proper motions.

Another potential issue with these faint sources is that they have poorer localizations than bright sources. The potential counterpart to CX16 is a faint UV source northeast of its error circle with a distance of $\approx 0.98''$ (or $\approx 1.84P_{\text{err}}$) from the nominal *Chandra* position, which suggests that it may be a chance coincidence. However, the *HST* lightcurve for CX16 reveals NUV_{336} variability on hours timescales (reduced $\chi^2 \approx 1.96$), suggesting a faint CV nature, since AGN tend to show less short-term variability. New *HST* imaging could reveal their PMs, testing an AGN hypothesis.

4.5 CX7 and CX13

Our suggested counterparts to CX7 and CX13 show moderately blue colors in $B_{435} - V_{555}$ (2004) and/or $V_{606} - I_{814}$ (2006) CMDs (see Fig. 3 and Tab. 4). The counterpart to CX13 (within the 95% error circle) was too faint to be detected in the 2012 WFC3 observations, so no proper mo-

tion is available for it. The counterpart to CX7 is outside the 95% error circle ($\approx 0.9''$, or $\approx 1.7P_{\text{err}}$, from the nominal *Chandra* position). Because it was only covered by the 2004 ACS/WFC observations, only limited information can be drawn from the photometry. Considering the lack of PM measurements for these sources, we conclude that they could either be CVs or AGNs.

4.6 CX9 and CX14

We found evolved stars that coincide with the error circles of CX9 and CX14. A red straggler (lying to the red of the giant branch; see Geller et al. 2017 for the definitions of red stragglers and sub-subgiants) and a subgiant are located in CX9's error circle, while a red giant is in CX14's error circle. The red straggler to CX9 was also detected in the Ksync photometry (2004 ACS/WFC observations; see Fig. 3) to have an obvious red excess. CX9 and CX14 may be RS Canum Venaticorum (RS CVn) variables, which are systems with an evolved primary (e.g. F/K type subgiant or K type giant) in a close binary, where the primary has active chromospheric regions that induce large stellar spots. The observed X-ray emissions in RS CVn stars are thought to originate from active coronal regions on the primary and/or the secondary star.

However, it is also possible that the evolved stars in these error circles are simply chance coincidences, or that the evolved stars have unseen compact companions. Considering the very low number of expected chance coincidences ($\approx 2.58 \times 10^{-4}$) for a red straggler to reside within the *Chandra* error circle, vs. a subgiant (with the number of chance coincidence $\approx 2.77 \times 10^{-2}$), we regard the red straggler as a highly likely optical counterpart of CX9. Red stragglers are rare, may be the product of mass transfer in a binary system, and have often been identified as X-ray sources (Belloni et al. 1998; Mathieu et al. 2003; Leiner et al. 2017). CX9 is a very interesting target for future observations, and fortunately, it is not affected by serious crowding in the core, which makes it resolvable with instruments that have even larger PSFs.

4.7 Estimate of XRBs and AGNs

The number of AGN expected within the half-light radius can be estimated using the empirical model with three power-law components from Mateos et al. (2008). Applying a soft (0.5–2.0 keV) flux limit of $S = 5.22 \times 10^{-16} \text{ erg s}^{-1} \text{ cm}^{-2}$, the model predicts that $N_{\text{AGN}}(> S) \approx 2^{+3}_{-1}$ (90% confidence limits are from Gehrels 1986) within the half-light radius. Thus, we expect that 14^{+1}_{-3} of our detected sources are likely members of M3, with CX12, and CX16 being plausible AGN (with no PM or P_{μ} available). CX8 does have a PM suggestive of a cluster member; however, further P_{μ} information is required for more secure identification. There are probably other AGNs among our X-ray sources without optical counterparts, which lie below our optical/UV detection limits.

Three confirmed MSPs (and one candidate) are known in M3, two with timing solutions and thus known positions (Hessels et al. 2007). The two known MSP positions do not correspond to any detected X-ray sources in our data. This is not surprising, since most MSPs observed in globular clusters have $L_X(0.3\text{--}8 \text{ keV})$ between $10^{30}\text{--}10^{31} \text{ ergs s}^{-1}$

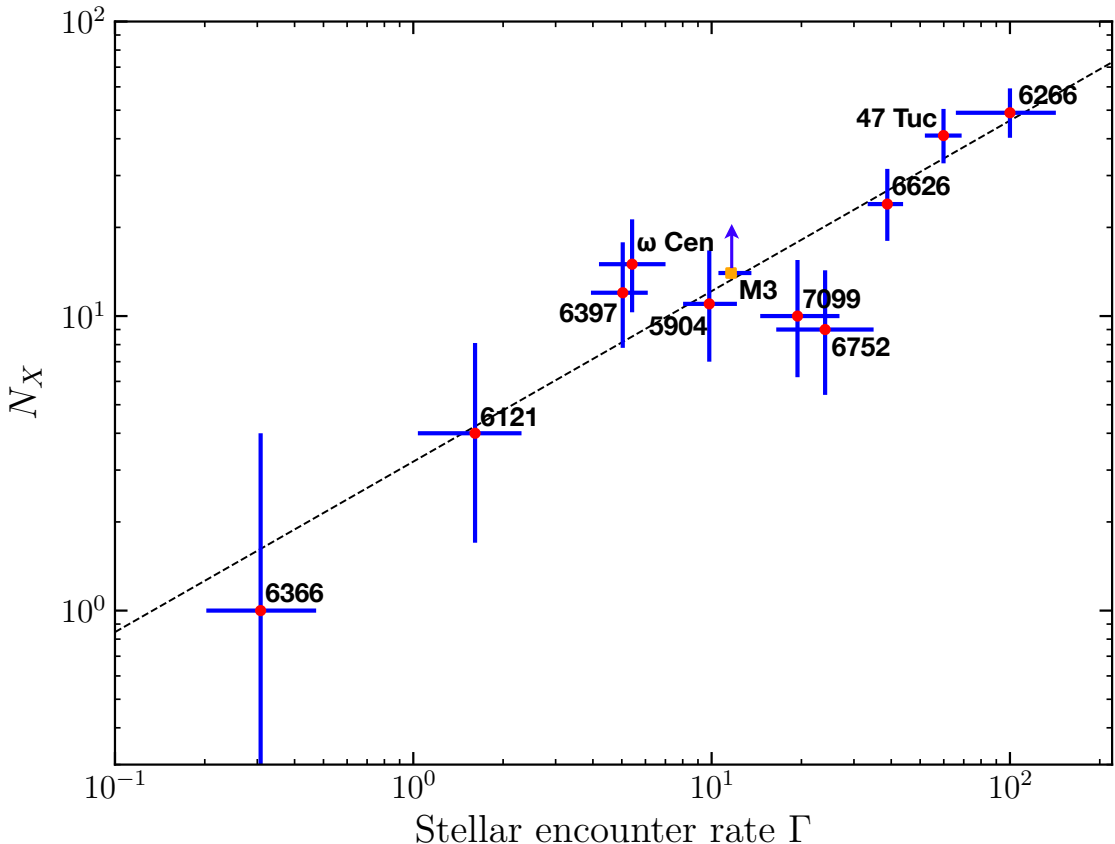


Figure 13. Number of non-AGN X-ray sources (N_X) in multiple GCs v.s. renormalised stellar encounter rates (Γ) from Bahramian et al. (2013). Γ s have been renormalised such that NGC 6266 has a Γ of 100. The lower limit inferred from our results of M3 is indicated with an orange square. The dashed line indicates the linear regression fit from Lugger et al. (2017).

(e.g. only 1 of 23 MSPs with known positions in 47 Tuc has $L_X > 10^{31}$ erg s $^{-1}$; Bogdanov et al. 2006; Ridolfi et al. 2016; Bhattacharya et al. 2017). Due to the larger distance to M3 (10.2 kpc; Harris 1996, 2010 version) and the relatively short exposures here, we do not have X-ray detections below $L_X \sim 1.3 \times 10^{31}$ erg s $^{-1}$. However, it is still possible that one of our X-ray sources might be an MSP with an unusually high X-ray luminosity.

We compared the number of X-ray sources we found in M3 with those from other GCs, and with the expected numbers of dynamically formed X-ray binaries. We used stellar encounter rates (Γ) from Bahramian et al. (2013), and numbers of non-AGN X-ray sources (N_X) in multiple GCs from Pooley et al. (2003) and Lugger et al. (2007). Since our luminosity limit ($L_{0.5-6.0} \approx 1.1 \times 10^{31}$ erg s $^{-1}$) is higher than Pooley's ($L_{0.5-6} = 4.0 \times 10^{30}$ erg s $^{-1}$), the N_X in M3 (14^{+1}_{-3}) reported here should be regarded as a lower limit. We compare our results of M3 with other GCs in Fig. 13 (where we have renormalised all Γ s so that Γ for NGC 6266 is 100), together with a linear regression fit ($N_X \propto \Gamma^{0.58 \pm 0.10}$) from Lugger et al. (2017). Deeper Chandra and HST observations would be helpful to verify the X-ray source content, and source classification, of M3. M3 will be a particularly helpful cluster, along with M13, M5, and ω Cen, in studying how lower-density clusters produce X-ray sources, as these clusters are likely to contain both primordial and dynamically-formed X-ray binaries.

5 CONCLUSIONS

Using ~ 30 ks of *Chandra* observations, we detected 16 X-ray point sources within the half-light radius of the globular cluster M3. The X-ray sources include the transient supersoft source and CV 1E1339, and a likely quiescent LMXB with a neutron star companion. Our optical/UV identification campaign has identified plausible optical and/or UV counterparts to 10 of 16 sources, including the previously identified 1E1339, a red straggler, a likely CV with unusually red optical colours, a faint red MS star to the qLMXB candidate, a possible giant (perhaps an RS CVn chromospherically active star), and five objects with UV and/or blue excesses, which may be CVs or AGNs.

ACKNOWLEDGEMENTS

We thank J. Anderson for making his KSYNC code available for our use, and for discussions. CH is supported by an NSERC Discovery Grant and a Discovery Accelerator Supplement. Our X-ray analyses are based on data obtained from the *Chandra* Data Archive, observations made by the *Chandra* X-ray Observatory and published previously in cited articles. Optical analyses are based on observations made with the NASA/ESA *Hubble Space Telescope*, obtained from the data archive at the Space Telescope Science Institute. STScI is operated by the Association of Uni-

versities for Research in Astronomy, Inc. under NASA contract NAS 5-26555. This work has made use of data from the European Space Agency (ESA) mission *Gaia* (<https://www.cosmos.esa.int/gaia>), processed by the *Gaia* Data Processing and Analysis Consortium (DPAC, <https://www.cosmos.esa.int/web/gaia/dpac/consortium>). Funding for the DPAC has been provided by national institutions, in particular the institutions participating in the *Gaia* Multilateral Agreement. This research has also made use of the NASA Astrophysics Data System (ADS) and software provided by the Chandra X-ray Center (CXC) in the application package CIAO.

REFERENCES

- Anderson J., et al., 2008, *AJ*, **135**, 2055
 Bahramian A., Heinke C. O., Sivakoff G. R., Gladstone J. C., 2013, *ApJ*, **766**, 136
 Bahramian A., Heinke C. O., Degenaar N., Chomiuk L., Wijnands R., Strader J., Ho W. C. G., Pooley D., 2015, *MNRAS*, **452**, 3475
 Bailyn C. D., Grindlay J. E., Garcia M. R., 1990, *ApJ*, **357**, L35
 Bassa C., et al., 2004, *ApJ*, **609**, 755
 Bassa C. G., Pooley D., Verbunt F., Homer L., Anderson S. F., Lewin W. H. G., 2008, *A&A*, **488**, 921
 Belloni T., Verbunt F., Mathieu R. D., 1998, *A&A*, **339**, 431
 Bhattacharya D., van den Heuvel E. P. J., 1991, *Phys. Rep.*, **203**, 1
 Bhattacharya S., Heinke C. O., Chugunov A. I., Freire P. C. C., Ridolfi A., Bogdanov S., 2017, *MNRAS*, **472**, 3706
 Bogdanov S., Grindlay J. E., Heinke C. O., Camilo F., Freire P. C. C., Becker W., 2006, *ApJ*, **646**, 1104
 Britt C. T., et al., 2014, *ApJS*, **214**, 10
 Camilo F., Rasio F. A., 2005, in Rasio F. A., Stairs I. H., eds, Astronomical Society of the Pacific Conference Series Vol. 328, Binary Radio Pulsars. p. 147 ([arXiv:astro-ph/0501226](https://arxiv.org/abs/astro-ph/0501226))
 Campana S., Stella L., Mereghetti S., Colpi M., Tavani M., Ricci D., Dal Fiume D., Belloni T., 1998, *ApJ*, **499**, L65
 Cash W., 1979, *ApJ*, **228**, 939
 Chakrabarty D., et al., 2014, *ApJ*, **797**, 92
 Clark G. W., 1975, *ApJ*, **199**, L143
 Cohn H. N., et al., 2010, *ApJ*, **722**, 20
 Cool A. M., Grindlay J. E., Cohn H. N., Lugger P. M., Slavin S. D., 1995, *ApJ*, **439**, 695
 Cool A. M., Grindlay J. E., Cohn H. N., Lugger P. M., Bailyn C. D., 1998, *ApJ*, **508**, L75
 Cool A. M., Haggard D., Arias T., Brochmann M., Dorfman J., Gafford A., White V., Anderson J., 2013, *ApJ*, **763**, 126
 Cox A. N., 2000, Allen's astrophysical quantities
 Dempsey R. C., Linsky J. L., Fleming T. A., Schmitt J. H. M. M., 1993, *ApJS*, **86**, 599
 Deustua S. e., 2016, WFC3 Data Handbook, Version 3.0 (Baltimore, MD: STScI)
 Dieball A., Rasekh A., Knigge C., Shara M., Zurek D., 2017, *MNRAS*, **469**, 267
 Dotani T., Asai K., Greiner J., 1999, *PASJ*, **51**, 519
 Edmonds P. D., Gilliland R. L., Heinke C. O., Grindlay J. E., 2003a, *ApJ*, **596**, 1177
 Edmonds P. D., Gilliland R. L., Heinke C. O., Grindlay J. E., 2003b, *ApJ*, **596**, 1197
 Edmonds P. D., Kahabka P., Heinke C. O., 2004, *ApJ*, **611**, 413
 Fabian A. C., Pringle J. E., Rees M. J., 1975, *MNRAS*, **172**, 15p
 Freire P. C. C., et al., 2017, *MNRAS*, **471**, 857
 Gaia Collaboration et al., 2016, *A&A*, **595**, A1
 Gaia Collaboration et al., 2018a, *A&A*, **616**, A1
 Gaia Collaboration et al., 2018b, *A&A*, **616**, A12
 Gehrels N., 1986, *ApJ*, **303**, 336
 Geller A. M., et al., 2017, *ApJ*, **840**, 66
 Gnedin O. Y., Zhao H., Pringle J. E., Fall S. M., Livio M., Meylan G., 2002, *ApJ*, **568**, L23
 Grindlay J. E., Hertz P., Steiner J. E., Murray S. S., Lightman A. P., 1984, *ApJ*, **282**, L13
 Grindlay J. E., Heinke C., Edmonds P. D., Murray S. S., 2001, *Science*, **292**, 2290
 Harris W. E., 1996, *AJ*, **112**, 1487
 Heinke C. O., Grindlay J. E., Lugger P. M., Cohn H. N., Edmonds P. D., Lloyd D. A., Cool A. M., 2003, *ApJ*, **598**, 501
 Heinke C. O., Grindlay J. E., Edmonds P. D., 2005a, *ApJ*, **622**, 556
 Heinke C. O., Grindlay J. E., Edmonds P. D., Cohn H. N., Lugger P. M., Camilo F., Bogdanov S., Freire P. C., 2005b, *ApJ*, **625**, 796
 Heinke C. O., Rybicki G. B., Narayan R., Grindlay J. E., 2006, *ApJ*, **644**, 1090
 Heinke C. O., et al., 2010, *ApJ*, **714**, 894
 Henze M., et al., 2009, *A&A*, **500**, 769
 Henze M., et al., 2011, *A&A*, **533**, A52
 Henze M., et al., 2013, *A&A*, **549**, A120
 Hertz P., Grindlay J. E., 1983, *ApJ*, **275**, 105
 Hertz P., Grindlay J. E., Bailyn C. D., 1993, *ApJ*, **410**, L87
 Hessels J. W. T., Ransom S. M., Stairs I. H., Kaspi V. M., Freire P. C. C., 2007, *ApJ*, **670**, 363
 Hills J. G., 1976, *MNRAS*, **175**, 1P
 Hong J., van den Berg M., Schlegel E. M., Grindlay J. E., Koenig X., Laycock S., Zhao P., 2005, *ApJ*, **635**, 907
 Huang R. H. H., Becker W., Edmonds P. D., Elsner R. F., Heinke C. O., Hsieh B. C., 2010, *A&A*, **513**, A16
 Ivanova N., Heinke C. O., Rasio F. A., Taam R. E., Belczynski K., Fregeau J., 2006, *MNRAS*, **372**, 1043
 Ivanova N., da Rocha C. A., Van K. X., Nandez J. L. A., 2017, *ApJ*, **843**, L30
 Jonker P. G., et al., 2011, *ApJS*, **194**, 18
 Jordán A., et al., 2004, *ApJ*, **613**, 279
 Jordán A., et al., 2007, *ApJ*, **671**, L117
 Kiel P. D., Hurley J. R., 2006, *MNRAS*, **369**, 1152
 Knigge C., Baraffe I., Patterson J., 2011, *ApJS*, **194**, 28
 Leiner E., Mathieu R. D., Geller A. M., 2017, *ApJ*, **840**, 67
 Lewin W. H. G., Joss P. C., 1983, in Lewin W. H. G., van den Heuvel E. P. J., eds, Accretion-Driven Stellar X-ray Sources. p. 41
 Lu T.-N., Kong A. K. H., Bassa C., Verbunt F., Lewin W. H. G., Anderson S. F., Pooley D., 2009, *ApJ*, **705**, 175
 Lucas R. e. a., 2016, ACS Data Handbook, Version 8.0 (Baltimore, MD: STScI)
 Lugger P. M., Cohn H. N., Heinke C. O., Grindlay J. E., Edmonds P. D., 2007, *ApJ*, **657**, 286
 Lugger P. M., Cohn H. N., Cool A. M., Heinke C. O., Anderson J., 2017, *ApJ*, **841**, 53
 Mateos S., et al., 2008, *A&A*, **492**, 51
 Mathieu R. D., van den Berg M., Torres G., Latham D., Verbunt F., Stassun K., 2003, *AJ*, **125**, 246
 Nardiello D., et al., 2018, preprint, ([arXiv:1809.04300](https://arxiv.org/abs/1809.04300))
 Peacock M. B., Maccarone T. J., Waters C. Z., Kundu A., Zepf S. E., Knigge C., Zurek D. R., 2009, *MNRAS*, **392**, L55
 Pecaut M. J., Mamajek E. E., 2013, *ApJS*, **208**, 9
 Pfahl E., Rappaport S., Podsiadlowski P., 2003, *ApJ*, **597**, 1036
 Pickles A. J., 1998, *PASP*, **110**, 863
 Piotti G., et al., 2015, *AJ*, **149**, 91
 Pooley D., Hut P., 2006, *ApJ*, **646**, L143
 Pooley D., et al., 2002, *ApJ*, **573**, 184
 Pooley D., et al., 2003, *ApJ*, **591**, L131
 Ransom S. M., Hessels J. W. T., Stairs I. H., Freire P. C. C., Camilo F., Kaspi V. M., Kaplan D. L., 2005, *Science*, **307**, 892

- Ridolfi A., et al., 2016, *MNRAS*, **462**, 2918
 Rivera Sandoval L. E., et al., 2018, *MNRAS*, **475**, 4841
 Rutledge R. E., Bildsten L., Brown E. F., Pavlov G. G., Zavlin V. E., 2002, *ApJ*, **578**, 405
 Saito Y., Kawai N., Kamae T., Shibata S., Dotani T., Kulkarni S. R., 1997, *ApJ*, **477**, L37
 Sarajedini A., et al., 2007, *AJ*, **133**, 1658
 Sirianni M., et al., 2005, *PASP*, **117**, 1049
 Sivakoff G. R., et al., 2007, *ApJ*, **660**, 1246
 Soto M., et al., 2017, *AJ*, **153**, 19
 Stacey W. S., Heinke C. O., Elsner R. F., Edmonds P. D., Weiskopf M. C., Grindlay J. E., 2011, *ApJ*, **732**, 46
 Stetson P. B., 1987, *PASP*, **99**, 191
 Thomson G. S., et al., 2012, *MNRAS*, **423**, 2901
 Verbunt F., 2003, in Piotto G., Meylan G., Djorgovski S. G., Riello M., eds, Astronomical Society of the Pacific Conference Series Vol. 296, New Horizons in Globular Cluster Astronomy. p. 245 ([arXiv:astro-ph/0210057](https://arxiv.org/abs/astro-ph/0210057))
 Verbunt F., Hut P., 1987, in Helfand D. J., Huang J.-H., eds, IAU Symposium Vol. 125, The Origin and Evolution of Neutron Stars. p. 187
 Verbunt F., Lewin W. H. G., 2006, Globular cluster X-ray sources. pp 341–379
 Verbunt F., Bunk W., Hasinger G., Johnston H. M., 1995, *A&A*, **300**, 732
 Verbunt F., Pooley D., Bassa C., 2008, in Vesperini E., Giersz M., Sills A., eds, IAU Symposium Vol. 246, Dynamical Evolution of Dense Stellar Systems. pp 301–310 ([arXiv:0710.1804](https://arxiv.org/abs/0710.1804)), doi:[10.1017/S1743921308015822](https://doi.org/10.1017/S1743921308015822)
 Watkins L. L., van der Marel R. P., Bellini A., Anderson J., 2015, *ApJ*, **812**, 149
 Zavlin V. E., Pavlov G. G., Sanwal D., Manchester R. N., Trümper J., Halpern J. P., Becker W., 2002, *ApJ*, **569**, 894

one can use similar method to find that

$$\alpha = -\frac{\left(\sum_i \frac{M_{2,i}^2}{\sigma_i^2}\right)\left(\sum_i \frac{D_i M_{1,i}}{\sigma_i^2}\right) - \left(\sum_i \frac{M_{1,i} M_{2,i}}{\sigma_i^2}\right)\left(\sum_i \frac{D_i M_{2,i}}{\sigma_i^2}\right)}{\left(\sum_i \frac{M_{1,i} M_{2,i}}{\sigma_i^2}\right) - \left(\sum_i \frac{M_{1,i}^2}{\sigma_i^2}\right)\left(\sum_i \frac{M_{2,i}^2}{\sigma_i^2}\right)}. \quad (\text{A5})$$

$$\beta = -\frac{\left(\sum_i \frac{M_{1,i}^2}{\sigma_i^2}\right)\left(\sum_i \frac{D_i M_{2,i}}{\sigma_i^2}\right) - \left(\sum_i \frac{M_{1,i} M_{2,i}}{\sigma_i^2}\right)\left(\sum_i \frac{D_i M_{1,i}}{\sigma_i^2}\right)}{\left(\sum_i \frac{M_{1,i} M_{2,i}}{\sigma_i^2}\right) - \left(\sum_i \frac{M_{1,i}^2}{\sigma_i^2}\right)\left(\sum_i \frac{M_{2,i}^2}{\sigma_i^2}\right)}.$$

This paper has been typeset from a TeX/LATEX file prepared by the author.

APPENDIX A: RENORMALIZATION OF SED MODELS WITH χ^2 MINIMIZATION METHOD

For a single component model, the χ^2 is defined as

$$\chi^2 = \sum_i \left[\frac{(M_i - D_i)}{\sigma_i} \right]^2, \quad (\text{A1})$$

where M_i and D_i are the model value and the data value at x_i , respectively, and α is a normalization factor. We want to find α such that

$$\frac{\partial \chi^2}{\partial \alpha} = 0. \quad (\text{A2})$$

Plugging eq.(A1), one can solve for α and find that

$$\alpha = \frac{\sum_i \frac{M_i D_i}{\sigma_i^2}}{\sum_i \frac{M_i^2}{\sigma_i^2}}. \quad (\text{A3})$$

For the case of an composite model with two additive components, i.e.

$$M = \alpha M_1 + \beta M_2, \quad (\text{A4})$$